Topological Phases in Narrow-band syste

by

Evelyn Tang

Submitted to the Department of Physics
in partial fulfillment of the requirements for the degree of

Doctor of Philosophy in Physics

at the

MASSACHUSETTS INSTITUTE OF TECHNOLOGY

September 2015

Signature redacted

Author ... .
Department of Physics
July 18, 2015

Signature redacted

Certified by.. .....
Xiao-Gang Wen
Cecil and Ida Green Professor of Physics
Thesis Supervisor

Signature redacted

Accepted by ... .
Nergis Mavalvala
Associate Department Head for Education and Professor of Physics

Topological Phases in Narrow-band systems

by

Evelyn Tang

Submitted to the Department of Physics
on July 18, 2015, in partial fulfillment of the
requirements for the degree of
Doctor of Philosophy in Physics

Abstract

I discuss several novel topological phases in correlated electron systems, realized through spin-orbit interactions and lattice effects especially narrow-band systems. The first realizes the fractional quantum Hall effect using geometric frustration and ferromagnetism to obtain a nearly flat band with a large bandgap and non-zero Chern number. This system can support this effect at high temperatures upon partial filling of the flat band. The second proposal builds upon this system: as the ground state is a fractional quantum Hall state, excitations of this state are anyons when there is an incommensurate filling. The underlying lattice allows access to a new regime in which the anyon gas can form a charged superfluid, including states with instrinsic topological order or that similar to a BCS-type state. The third proposal studies topological crystalline insulators and strain as an effective gauge field on the surface state Dirac fermions. The zero-energy Landau orbitals form a flat band where the high density of states gives rise to the interface superconductivity observed in IV-VI semiconductor multilayers at high temperatures, with non-BCS behavior. A discussion of superconductivity in flat band systems concludes and is contrasted with classic results for a typical electron gas. This work closely parallels that in references [1, 2, 3].

Thesis Supervisor: Xiao-Gang Wen
Title: Cecil and Ida Green Professor of Physics

Acknowledgments

My first words go to my advisor, Xiao-Gang, who taught me what it means to be a scientist. Through our projects, I learnt an openness to unexpected outcomes or apparent mistakes to see what we could learn. From our discussions, I developed a rigor in asking scientific questions, and an unflagging enthusiasm for the beauty of reality or what our research could point towards. Next of all, Liang, with whom I had the great good fortune to work with in the later part of my graduate work. Liang's contagious joy and energy in discovery, his unfailing intuition for a good lead to pursue, and his simple friendliness made our work together light, fast, and a blast.

Several of the MIT faculty have been constantly supportive and veritable fonts of wisdom when called upon — Patrick, with whom I did my first research project, and Senthil, my patiently encouraging academic advisor — both also dispensed much needed practical advice and kindly smiles when I was confused. Joe, who with his cheerfulness and passionate curiosity, was such a pleasure to have on my thesis committee. Young, Mehran, Jeremy, and Marin were all faculty with whom I interacted with on occasion to my own great benefit. Other professors outside of condensed matter like Krishna, Ed and Jackie have also been helpful with useful suggestions and the right words in key moments. Very importantly, my dear mentor Hazel Sive taught me in words and example how to hold my own ground in good scholarly style and personal acumen.

My time at MIT was largely shaped by the wonderful and brilliant peers I was fortunate to interact with daily: the other graduate students who began with me like David, Drew, Andrea, Javier and Rahul, were the bedrock of my experience and education. The countless hours of discussion and shared moments sharpened my way of thinking and contributed to my outlook on life. Chong, Maksym, Justin, Karen and other students or postdocs also made a tremendous difference in my graduate school career through their friendship and solidarity.

I could not have completed this step without the love of my dear family and several wonderful friends. My family has been nothing but supportive and selfless in

their encouragement of my work; patient and quick to help where possible. So many friends who kept me going through difficult and bleak moments, Jose, Elvira, Paolo and others, are too numerous to name.

I am grateful to all these people in the past and present, for helping and holding me through this journey, which has been a great adventure and opportunity for me.

Contents

List of Figures

Chapter 1

Introduction

Topological phases are new states of matter with unconventional properties, such as an unusual edge (or boundary of the material sample). Topology has typically denoted the mathematical study of spaces and shapes, and more recently turned out extremely useful in physics, such as to describe the winding of an electron's wavefunction. Remarkably, subtle changes to the topology of the electron's wavefunction (which may appear as just additional complex phases), can give rise to different physical states. Such states are often accompanied by clear visible signatures that help them to be distinguished experimentally.

For decades, the main realization of topological phases were the integer and fractional quantum Hall effects (IQHE and FQHE respectively). These landmark discoveries made in the 1980s became favorite and well-examined experiments, in their host semiconductor systems of two-dimensional electron gases (2DEGs). In this thesis, we discuss an extension of the FQHE in a completely different system from semiconductors, by mimicking the relevant properties of this state such as a flat band. This is discussed in chapter two.

The FQHE remains beloved by many physicists because of its fascinating properties. It is a strongly correlated state, containing quasiparticles (gapped collective excitations) with unusual statistics. The existence of this state in two-dimensions allows these quasiparticles to possess intricate braiding statistics and host additional exotic topological phases. The proposal we introduced of the FQHE on a lattice gives

rise to a new regime, in which these quasiparticles can interact to form an anyon superfluid. The formalism we develop to describe such a state reveals a unique algebra between new types of quasiparticles – as shown in chapter three.

Our knowledge of materials and experimental systems that support such phases received a huge boost with the discovery of topological insulators this past decade. These systems provide analogs and a generalization to other dimensions, while retaining several commonalities including anomalous edges (e.g. that are chiral), and twisting of the electron wavefunction. In chapter four we explore a new class of such materials, topological crystalline insulators, that additionally utilize crystal symmetry for protection of its topological properties. In particular, lattice effects combine with the surface states to result in partially flat bands. This supports an entirely new state, superconductivity, the origin of which is otherwise difficult to explain in these systems.

In these examples, the combination of lattice effects and flat bands can give rise to radically new states, often because interaction effects dominate in a flat band (over the kinetic energy). In chapter five we see this unusual regime gives a new prediction for the renormalization of the Coloumb repulsion in a superconductor. In the limit of a partially flat band, we obtain a result governed now by the flatband bandwidth, which modifies the classic result for an electron gas (as obtained by Anderson, Morel and others).

1.1 Topological phases

The standard theoretical concept in the classification of phases and transitions between them, has been that of Landau symmetry breaking[5, 6]. However, this theory turned out to be inadequate when the fractional quantum Hall (FQH) state[7, 8] was discovered. Such highly-entangled quantum states are not distinguished by any symmetries as that framework had dictated, but are characterized by new topological quantum numbers such as a ground state degeneracy[9, 10] and non-Abelian Berry's phases[11] of the ground states[12]. The robustness of these quantum numbers is

topologically protected, i.e. only global (e.g. macroscopic) and not local changes can destroy them.

The new kind of order revealed in these topological quantum numbers is named topological order.[12, 13] Recently it was realized that topological order can be interpreted as patterns of long-range quantum entanglement[14, 15, 16]. This entanglement has important applications for topological quantum computation: the robust ground state degeneracy can be used as quantum memory[17]. Fractional defects from the entangled states which carry fractional charges[8] and fractional statistics[18, 19, 20] (or non-Abelian statistics[21, 22]) can be used to perform fault tolerant quantum computation[23, 24].

1.2 New advances and materials

The past decade has seen the discovery of a new group of materials exhibiting such topological phases, driven instead by spin-orbit coupling, called topological insulators[25]. Similar to quantum Hall states, topological insulators are gapped systems that contain gapless states on the surface or the edge in two dimensions. However unlike quantum Hall states, they require the existence of a given symmetry (such as time-reversal) to protect their topological nature, without which the state would simply be an ordinary insulator. The existence of these states and their Dirac edge modes were demonstrated experimentally using angle-resolved photoemission spectroscopy.

Even more recently proposed and discovered, topological crystalline insulators host novel topological surface states that are protected by the symmetry of the underlying crystal[26, 27, 28, 29]. At low carrier energy, these surface states consist of multi-valley massless Dirac fermions, whose characteristic properties are highly tunable by external perturbations. Breaking the crystal symmetry at the atomic scale generates a Dirac mass and leads to gapped phases[26, 30] with potentially novel functionalities in low-power electronics and spintronics[31, 32, 33].

A main focus of this thesis is to explore the interplay of complex mathematical

structures that predict such states with physical systems – by considering lattice structures and the interactions between electrons. In particular I studied fractional quantum Hall and superconducting states in topological systems.

One example of this is the proposal of fractional Chern insulators, in chapter two. In the FQHE, many electrons cooperate to form a state whose excitations carry a fraction of the fundamental charge and fractional statistics. While this physics has been seen until now only in very clean 2DEGs and graphene at high magnetic fields and extremely low temperatures, we proposed it can also be realized in lattice systems at much higher temperatures and more accessible conditions. We achieved this by devising an analog of every needed ingredient, in particular to note the right combination that could give rise to a flat band.

1.3 With lattice effects: novel states

Furthering the dialogue between theory and realistic systems can allow us to design new states or shed light on mysterious physical phenomena. For instance, interface superconductivity in the IV-VI semiconductors was a long-standing puzzle that could not be adequately explained by traditional methods. In this thesis, I developed a more comprehensive theory by combining lattice properties and interactions between electrons within a topological framework.

An example is that of intrinsic topological superconductivity. Flat bands supporting the FQHE would contain excitations with fractional statistics, and we became curious about what ground state such particles would form — as neither a Fermi liquid or a Bose-Einstein condensate are certain. Further, the underlying lattice now allows for finite kinetic energy for the excitations, unlike in 2DEGs where the completely flat band would only have localized excitations. Upon investigation, we found that a finite density of such excitations could condense into a superconducting state — one with extremely unusual topological order and driven purely by strong repulsions.

This new gapped topological order comes together with a gapless (superfluid) mode, so we had to extend the usual tools of K-matrix theory (for describing gapped

topological order) to this context. To do this we isolated a gapped sector in which quasiparticles $\{\psi_l\}$ can be identified using a set of l-vectors and their statistics calculated with

$$\theta_l = \pi l^T K^{-1} l. \tag{1.1}$$

Moving a quasiparticle excitation around an electron excitation ψ_e induces a phase of multiple 2π, a useful criteria to distinguish between the trivial and fractional quasiparticles emergent in the system. The different emergent quasiparticles and the particular algebra between them are signatures of the new topological order we found — distinct from the bosonic topologic order characteristic of purely fractional quantum Hall systems.

Another example is of interface superconductivity in topological crystalline insulators (TCIs). Topological theories can provide a more complete description of experiments, particularly in the case we studied of interface superconductivity in IV-VI semiconductors. After identifying the materials as TCIs, it was crucial to observe that strain caused by dislocations could act on the surface Dirac fermions to macroscopically alter the electronic properties. This is unusual as strain due to dislocations is often viewed as an uncontrollable or messy contribution, instead we showed that the spontaneous formation of a regular dislocation array actually contributed to partially flat bands forming across the system. The large density of states from these partially flat bands favor superconductivity with a non-BCS dependence of Tc — which is in good agreement with the experimentally observed variation of Tc with the dislocation array period.

1.4 Flat bands open new possibilities

Evidently, the study of flat bands is motivated from various angles. While quite simply they can mimic Landau levels and support states in which interaction effects dominate, our work has found that flat bands enable a variety of new states and

effects. Existing topological phases in combination with such novel platforms interact in surprising ways to give results qualitatively different from those in former regimes. This suggests much potential for future work in the intersection of strong lattice effects, especially flat bands, with novel topological phases.

Chapter 2

High temperature fractional quantum Hall states

We show that a suitable combination of geometric frustration, ferromagnetism and spin-orbit interactions can give rise to nearly flat bands with a large bandgap and non-zero Chern number. Partial filling of the flat band can give rise to fractional quantum Hall states at high temperatures (maybe even room temperature). While the identification of material candidates with suitable parameters remains open, our work indicates intriguing directions for exploration and synthesis.

2.1 Desirability of FQH states at high temperatures

Presently, highly entangled gapped phases in FQH systems[7, 8] are only realized at very low temperatures. Here we present a proposal to realize these states at high temperatures (even room temperature). The ideal is to combine spin-orbit coupling, ferromagnetism, and geometric frustration. Both spin-orbit coupling and ferromagnetism can have high energy scales and can appear at room temperature. In some cases, combining them leads to energy bands with non-zero Chern numbers and filling such an energy band will give rise to integer quantum Hall states. Further, in geometrically frustrated systems — lattices on which hopping is frustrated — some of these topologically non-trivial energy bands can be very flat[34, 35]. These would

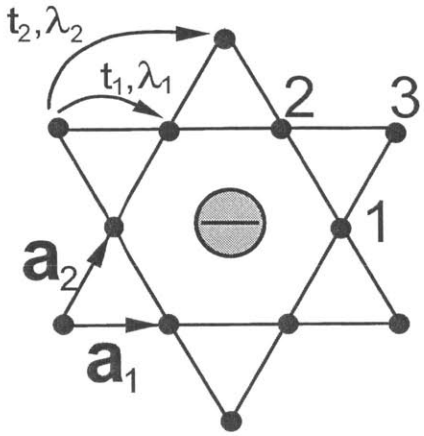

Figure 2-1: The kagome lattice is a triangular Bravais lattice with a 3-point basis labelled $l = 1, 2, 3$; $\mathbf{a}_1 = \hat{x}$ and $\mathbf{a}_2 = (\hat{x} + \sqrt{3}\hat{y})/2$ are the basis vectors. In the metallic kagome lattice Fe_3Sn_2, spin-orbit coupling arises from the electric field due to the Sn ion at the center of the hexagon.

mimic Landau levels in free space. When such a flat band with a non-zero Chern number is partially filled (such as 1/3 or 1/2 filled), FQH states can appear. Here we study a simple example of this idea on the geometrically frustrated kagome lattice.

Several aspects of these ideas have been active in recent research. Spin-orbit coupling can lead to a topological insulator in various geometrically frustrated systems,[36, 37, 38, 39] and non-collinear magnetic order can lead to integer quantum Hall states.[40, 37] Alternatively, interactions in geometrically frustrated systems can break time-reversal symmetry[41, 42, 43, 44, 45, 46, 47, 48, 49] which again can give rise to integer quantum Hall states. Here we show that an extension of these ideas may set the stage for FQH states and other highly entangled states with fractional statistics and fractional charges — possibly even at room temperature.

2.2 Nearly flat band; non-zero Chern number

We consider nearest and next-nearest neighbor hopping on a kagome lattice with spin-orbit interactions in the Hamiltonian

$$H = -t_1 \sum_{\langle ij\rangle\sigma} c^\dagger_{i\sigma} c_{j\sigma} + i\lambda_1 \sum_{\langle ij\rangle\alpha\beta} (\mathbf{E}_{ij} \times \mathbf{R}_{ij}) \cdot \boldsymbol{\sigma}_{\alpha\beta} c^\dagger_{i\alpha} c_{j\beta}$$
$$-t_2 \sum_{\langle\langle ij\rangle\rangle\sigma} c^\dagger_{i\sigma} c_{j\sigma} + i\lambda_2 \sum_{\langle\langle ij\rangle\rangle\alpha\beta} (\mathbf{E}_{ij} \times \mathbf{R}_{ij}) \cdot \boldsymbol{\sigma}_{\alpha\beta} c^\dagger_{i\alpha} c_{j\beta} \tag{2.1}$$

where $c^\dagger_{i\sigma}$ creates an electron with spin σ on site $\mathbf{r}_i$. Here $\langle ij\rangle$ denotes nearest neighbors and $\langle\langle ij\rangle\rangle$ next-nearest neighbors. The second and fourth terms are time-reversal invariant and describe spin-orbit interactions.$\mathbf{R}_{ij}$ is the distance vector between sites i and j and $\mathbf{E}_{ij}$ the electric field from neighboring ions experienced along $\mathbf{R}_{ij}$.

To obtain FQH states we need to break time-reversal symmetry. This is likely to happen spontaneously from exchange effects in the flat band that cause ferromagnetism[41, 42, 43]. Alternatively, one can apply an external magnetic field or couple the system to a ferromagnet. In the extreme limit the electron spins are totally polarized within the partially filled band — the case we examine here. Hence we consider spin-orbit coupling that also conserves S_z, i.e. the electric field on each site is in the 2D plane. First studying just nearest-neighbor hopping ($t_2 = \lambda_2 = 0$), in momentum-space Eq. 2.1 is

$$H_{\mathbf{k}} = -2t_1 \begin{pmatrix} 0 & \cos k_1 & \cos k_2 \\ \cos k_1 & 0 & \cos k_3 \\ \cos k_2 & \cos k_3 & 0 \end{pmatrix}$$
$$\pm\ i2\lambda_1 \begin{pmatrix} 0 & \cos k_1 & -\cos k_2 \\ -\cos k_1 & 0 & \cos k_3 \\ \cos k_2 & -\cos k_3 & 0 \end{pmatrix} \tag{2.2}$$

where $\mathbf{a}_1 = \hat{x}$, $\mathbf{a}_2 = (\hat{x} + \sqrt{3}\hat{y})/2$, $\mathbf{a}_3 = \mathbf{a}_2 - \mathbf{a}_1$ and $k_n = \mathbf{k} \cdot \mathbf{a}_n$. We use units where the hopping parameter $t_1 = 1$. The $+(-)$ sign refers to spin up (down) electrons;

from here we focus on just the spin up electrons.

The spectrum consists of three energy bands and is gapless at $\lambda_1 = 0, \pm\sqrt{3}$. At all other points the spectrum is gapped and the top and bottom bands have unit Chern number with opposite sign while the middle band has zero Chern number. The Chern number is defined as[50]

$$c = \frac{1}{2\pi}\int_{BZ} d^2k F_{12}(k) \tag{2.3}$$

where $F_{12}(k)$ is the associated field strength given by $F_{12}(k) = \frac{\partial}{\partial k_1}A_2(k) - \frac{\partial}{\partial k_2}A_1(k)$ with the Berry connection $A_\mu(k) = -i\langle n_{\mathbf{k}}\frac{\partial}{\partial k_\mu}\rangle n_{\mathbf{k}}$. In the above $\rangle n_{\mathbf{k}}$ is a normalized wave function of the respective band.

Focusing on the lowest band which has a non-zero Chern number, we look for where this band is very flat compared to the bandgap and the energy scale of interactions. We denote W as the maximum bandwidth of the lowest band, Δ_{12} as the minimum bandgap between the two lowest bands and U as the strength of electron-electron interactions. When $U \gg W$, interaction effects dominate kinetic energy and partially filling the flat band would favor the Laughlin state.[8] Since band mixing could destroy band flatness, ideally $\Delta_{12} \gg U$. Hence we aim to maximize the ratio Δ_{12}/W in order to obtain FQH states. As the middle band has zero Chern number, any mixing between only two of the bands would not change the Chern number of the lowest band. If the lowest band remains flat even with mixing then Δ_{13}, the minimum bandgap between the lowest and highest bands, (and consequently the ratio Δ_{13}/W) is also of interest.

We find that $W \geq \Delta_{12}$ always — as the bandwidth vanishes so does the bandgap between the two lower bands (topological symmetry in real-space[51]), see Fig. 2-2. Here we show the band structure for $\lambda_1 = 1$ where $W = 1.3$ and $\Delta_{13}/W = 3.7$. As $\Delta_{12}/W \leq 1$ always, the spectrum does not have a clear separation of energy scales. When interactions are on the order of W, the bands will mix. This scenario is quite different from Landau levels in free space that are flat and well-separated, which could be due to limitations of this simplest model.

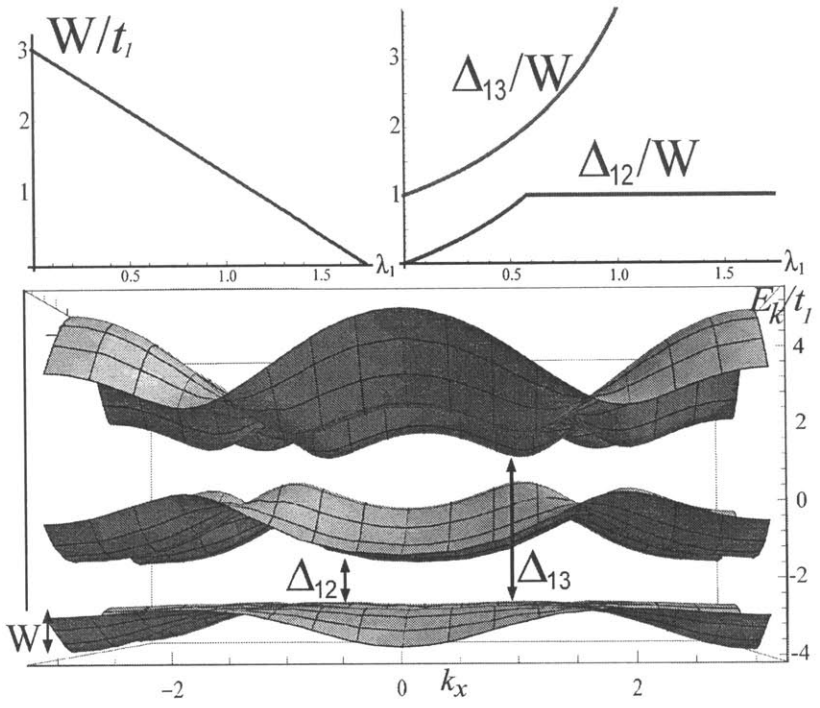

Figure 2-2: Results for nearest neighbor hopping as a function of λ_1 (nearest neighbor spin-orbit coupling). The bandwidth of the lowest band W vanishes at $\lambda_1 = \sqrt{3}$; however $W \geq \Delta_{12}$ always where Δ_{12} is the bandgap between the two lowest bands. Here we show the band structure for $\lambda_1 = 1$ where $W = 1.3$ and $\Delta_{13}/W = 3.7$. The spectrum does not have a clear separation of energy scales between Δ_{12}, W and U, the interaction strength, which could be due to limitations of the nearest neighbor hopping model.

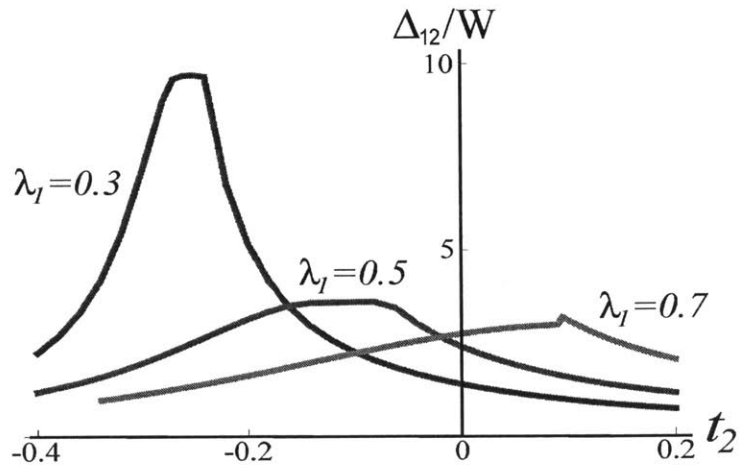

Figure 2-3: With the inclusion of next-nearest neighbor hopping, we obtain much higher bandgap to bandwidth ratios. We choose three values of $\lambda_1 = \lambda_2 = 0.3, 0.5$ and 0.7, and sweep Δ_{12}/W with t_2. For lower values of spin-orbit coupling, the ratio peaks at negative t_2; for relatively higher values of spin-orbit coupling the converse is true.

For a more realistic scenario we include second-nearest neighbor hopping which adds terms in the Hamiltonian

$$\begin{aligned} H_{\mathbf{k}} &= -2t_2 \begin{pmatrix} 0 & \cos(k_2+k_3) & \cos(k_3-k_1) \\ & 0 & \cos(k_1+k_2) \\ & & 0 \end{pmatrix} \\ &+ i2\lambda_2 \begin{pmatrix} 0 & -\cos(k_2+k_3) & \cos(k_3-k_1) \\ & 0 & -\cos(k_1+k_2) \\ & & 0 \end{pmatrix} \end{aligned} \tag{2.4}$$

In this larger parameter space the band maxima and minima are no longer fixed at the same symmetry points. We find that the largest values of Δ_{12}/W (and Δ_{13}/W) occur when λ_1 and λ_2 are of the same sign – in which case the results are symmetric under changing signs of both λ's in this spin polarized case. In Fig. 2-3, Δ_{12}/W is plotted as a function of t_2 for three values of $\lambda_1 = \lambda_2$. We see that at negative values of t_2 a lower spin-orbit coupling is needed; while for positive values of t_2 higher values of spin-orbit coupling would maximize the bandgap to bandwidth ratio.

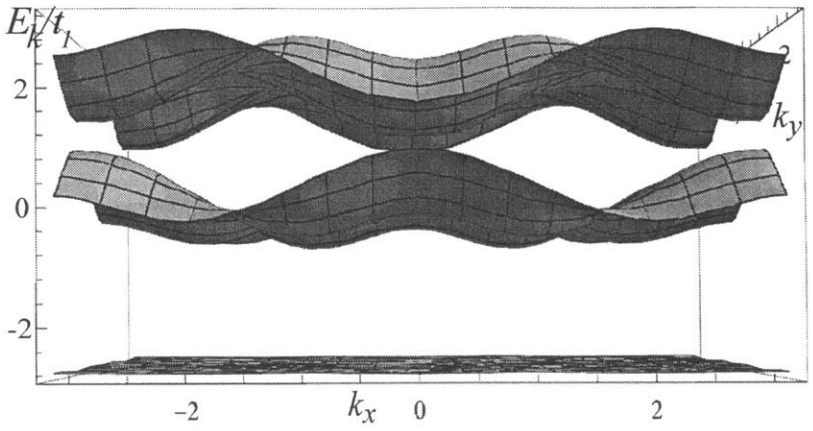

Figure 2-4: A very flat lowest band — well-separated from the two higher bands — is obtained with the parameters $t_2 = -0.3$, $\lambda_1 = 0.28$ and $\lambda_2 = 0.2$ (Case 1). The bandgap to bandwidth ratios are high: $\Delta_{12}/W = 52$ and $\Delta_{13}/W = 99$ respectively.

We present two examples where Δ_{12}/W and Δ_{13}/W reach high values at $t_2 = -0.3$. In Case 1, setting $t_2 = -0.3$, $\lambda_1 = 0.28$ and $\lambda_2 = 0.2$, we obtain a very flat lowest band separated from the two higher bands by a large gap (see Fig. 2-4). The values of Δ_{12}/W and Δ_{13}/W are 52 and 99 respectively. In another example, all three bands are fairly flat (particularly the lowest one) and mutually well-separated. The parameters used are $t_2 = -0.3, \lambda_1 = 0.6$ and $\lambda_2 = 0$. In Case 2, we obtain $\Delta_{12}/W = 8.7$ and $\Delta_{13}/W = 24$ respectively (see Fig. 2-5).

Calculating the Chern number c of the lowest flat band in these two cases, we find it is 1. This is expected as slowly turning off t_2 and λ_2 does not close the bandgap — and we have previously seen that in the absence of next nearest-neighbor hopping, the lowest band always has unit Chern number. When $\Delta \gg U \gg W$ is satisfied, partial filling of this flat band would favor the FQH state.

The distribution of the field strength $F_{12}(k)$ in the Brillouin zone is plotted in Fig. 2-6. We observe there are no singularities or very sharp features but $F_{12}(k)$ varies fairly smoothly especially in the first case with the flatter band. The presence of singularities — e.g. localized at the Dirac point — would have signalled a new (and much larger) length scale in the system. In our case, both the magnetic length scale (arising from spin-orbit interactions) and the variation of field strength $F_{12}(k)$ are on

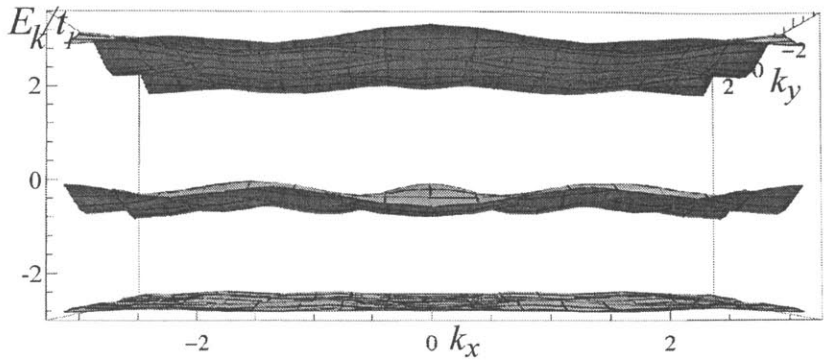

Figure 2-5: Three fairly flat bands are mutually well-separated with bandgap to bandwidth ratios of $\Delta_{12}/W = 8.7$ and $\Delta_{12}/W = 24$. Parameters used are $t_2 = -0.3, \lambda_1 = 0.6$ and $\lambda_2 = 0$ (Case 2).

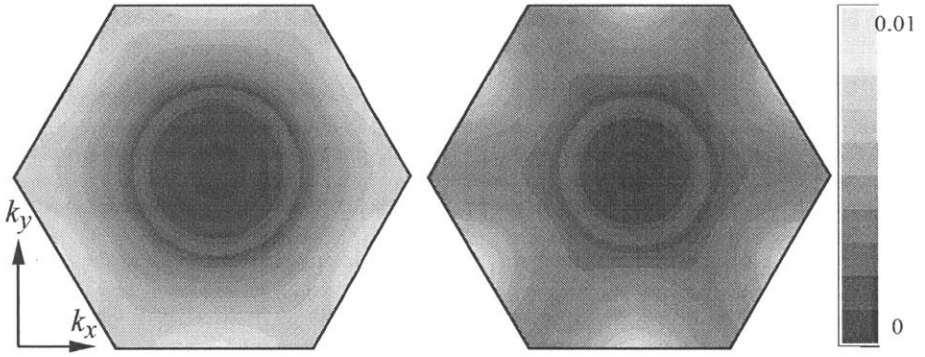

Figure 2-6: Distribution of the field strength $F_{12}(k)$ (Eq. 2.3) in the Brillouin zone for the flat bands in Cases 1 and 2 discussed above. They do not contain sharp features — especially Case 1 with the flatter band — hence the magnetic length scale remains on the order of the lattice constant a.

the order of the lattice constant a.

Thus the interaction energy scale is generated from the lattice constant a: $U \sim e^2/\epsilon a$ where ϵ is the dielectric constant. For a 1/3 filled flat band, analogous to results from FQH states in semiconductor-based systems[52] the gap for this $\nu = 1/3$ state is roughly $0.09e^2/\epsilon a = 500$K. (We choose $\epsilon = 3$ and $a = 10$; a is defined as the square root of the unit cell area). As the interaction energy scale is a hundred times larger than in semiconductors, we may see the FQH effect at room temperature. As band gaps Δ_{12} and Δ_{13} are easily much higher than room temperature, a fully filled band

could give the integer quantum Hall state at unusually high temperatures too.

2.3 Materials realization

We see that a suitable combination of geometric frustration, ferromagnetism and spin-orbit interactions can give rise to nearly flat bands with a large bandgap and non-zero Chern number. The ferromagnetism can arise from an external magnetic field, a ferromagnetic substrate for a thin film sample, and/or exchange effects. If the flat band is close to the Fermi energy, partial filling of the flat band can be controlled by doping and give rise to FQH states at high temperatures.

The choice of parameters in our calculations is based on known values of spin-orbit coupling. For example, in Herbertsmithite (a common copper-based 2D kagome lattice) the spin-orbit interaction is 8% of the kinetic energy.[53] Other compounds with 4d or 5d orbitals (instead of 3d as in Cu) may experience a larger spin-orbit interaction. For instance, the strength of spin-orbit coupling in Iridium-based kagome compounds can be on the order of magnitude of the kinetic energy, hence the substitution with 4d or 5d atoms in metallic kagome lattices could result in hopping parameters similar to the ones used in our work. Alternatively, making thin films of frustrated lattices with 4d or 5d atoms may lead to a flat band with strong spin-orbit coupling, where exchange effects in this flat band could cause ferromagnetism.

Most existing kagome compounds are Cu-based insulators. Some 2D kagome lattices show metallic behavior, for instance Fe_3Sn_2[54, 55] which shows ferromagnetism along the c-axis above 60K and in the kagome plane below 60K. Also, as spin-orbit interactions can be simulated in cold atom systems,[56, 57] it is possible to realize our hopping model in such systems. This would provide a method to obtain FQH states in cold atom systems.

In short, flat bands with non-zero Chern number arise in the examples we have given and in other geometrically frustrated systems with suitable levels of spin orbit interaction. By partially filling these bands e.g. via doping, one can expect the emergence of FQH states at high temperatures. While the identification of exact material

candidates remains open, our work indicates intriguing directions for synthesis and development.

During the publication of our work, we learned that T. Neupert et. al[58] also discussed the possibility of the FQH effect in interacting two-band lattice systems, while K. Sun et. al[59] found flat bands with non-zero Chern numbers on various lattices (including the kagome lattice) after including some complex hopping.

Chapter 3

Superconductor with intrinsic topological order in a flat band system

The previous chapter showed that in certain lattice systems, at commensurate filling fractions the ground state is a fractional quantum Hall state. The excitations of this state are anyons, and we explore what happens at incommensurate fillings, as the presence of the underlying lattice allows access to an entirely new regime where the anyon kinetic energy can be larger than their interaction energy. In this case, the resulting anyon gas can form a charged superfluid. This is studied with a flux attachment scheme, first using mean-field then adding fluctuations. We present three possible outcomes, the first two with intrinsic topological order, i.e. containing fractionalized quasiparticles that have a fusion structure of $(\mathbb{Z}_2)^4$ *and* $(\mathbb{Z}_8)^2$ *respectively. The third outcome has no fractionalized excitations similar to a BCS-type state; all three have intriguing implications and represent a mechanism for superconductivity driven purely by strong repulsion.*

3.1 New regime for FQH systems on lattice

The previous chapter provided a proposal for the fractional quantum Hall (FQH) effect to be realized in a lattice system, for instance in a flat band with spin-orbit coupling and spin polarization [1, 59, 58]. At commensurate filling fractions of this flat band, e.g. 1/3, it has been shown numerically that the ground-state in such systems is a FQH state [60, 61]. A natural question is what happens at incommensurate fillings, when the electron density is doped slightly away from a rational fraction and anyon excitations created.

The presence of the underlying lattice system allows us to access an entirely new regime where the anyon excitations may have kinetic energy larger than their interaction energy. This is in contrast to the FQH state in semiconductor systems, where electrons have zero bandwidth and anyons have a magnetic length scale several orders of magnitude larger than in lattice systems. Consequently, the anyon wavefunction is just a small perturbation to the electron wavefunction and is also expected to have very little dispersion, favoring localization or Wigner crystal formation. On a lattice system, anyons have a magnetic length scale on the order of the lattice spacing [1] and form a strong local charge distortion, resulting in an anyon hopping governed by the typical electron hopping energy.

We provide a more detailed discussion and comparison of energy scales in the Appendix, where the relevant anyon energy scales are estimated as $\sim \hbar^2/m_a l_a^2$ for the kinetic and $\sim (e/3)^2/\epsilon l_a$ for the interaction energy (m_a and l_a are an effective anyon mass and interparticle spacing, ϵ gives the effective screening, e.g. the dielectric constant of the substrate). Note that the anyon kinetic energy is an energy scale distinct from the bandwidth of the electron flat band, as the latter is a delicate balance of several different hopping parameters on a frustrated lattice; furthermore anyons reside on a separate unfrustrated lattice (e.g. Fig. 3-1(a)). When the anyon kinetic energy dominates over the anyon interaction energy, we obtain an anyon gas (while in the opposite limit we expect the anyons to form a Wigner crystal, or a hierachy FQH state at appropriate commensurate densities).

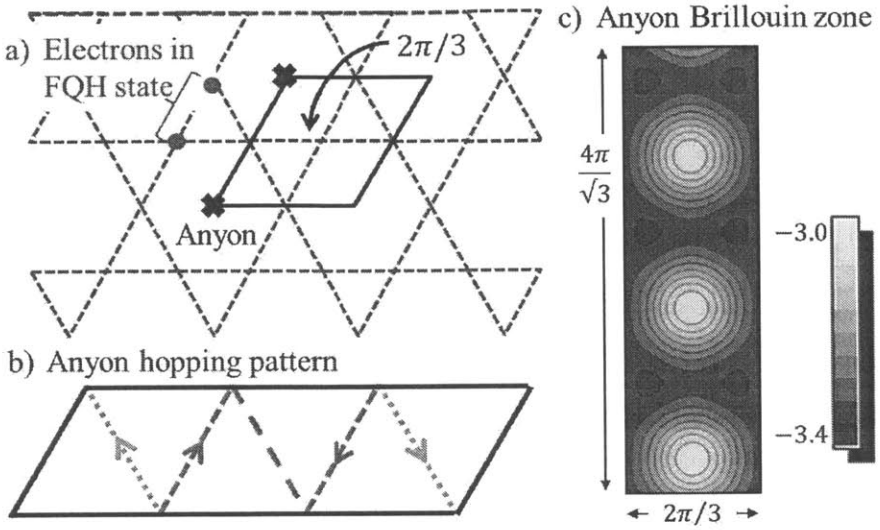

Figure 3-1: (a) Anyons live in the center of the hexagons of the kagome lattice (dashed red lines) to minimize repulsion with the electrons, and see a flux of $2\pi/3$ per unit cell (solid black line). (b) The anyons hop on an effective triangular lattice (lattice spacing set to unit width). The $2\pi/3$ flux breaks translation symmetry by three; here we illustrate a hopping configuration with uniform flux. In addition to regular $t = -1$ hopping (solid black lines), a phase of $\pi/3$ is added to the dotted (green) lines in the direction of the arrow, while $2\pi/3$ is added to the short dashed (blue) lines with π added on the wide dashed (red) line. (c) Resulting band structure of the lowest band with six degenerate minima.

To study the ground state of this anyon gas, we use a flux attachment scheme first in a mean-field approximation then with fluctuations, to find an anyon superfluid. As the anyons are charged, this would be a superconductor in the presence of an external electromagnetic field. Anyon condensation was first suggested by Laughlin in 1988 [62, 63] and explored by several authors [64, 65]. Here we present a system which provides the novel possibility of the right energy regime to support such physics.

Our formalism allows some choices so here we present three different scenarios. In the first two, we find that the superfluid contains quasiparticle excitations with fractionalized statistics, in one case with a fusion structure of $(\mathbb{Z}_2)^4$ and the other with $(\mathbb{Z}_8)^2$. Besides these examples of intrinsic topological order, we also present a third one with purely local excitations, very similar to a BCS-type superconducting state. The properties and implications of these scenarios are intriguing, and provide

a mechanism for superconductivity driven purely by strong repulsion.

3.2 Host system

We illustrate this on a kagome lattice system with spin-orbit coupling and time-reversal symmetry breaking (Chapter 2). A $\nu = 1/3$ FQH state in such a system has anyon excitations, so a finite density of anyons is expected to be created with a small amount of doping (small relative to total electron density). In order to minimize Coulomb repulsion with the electrons that live on the kagome lattice, these anyons would reside in the center of the hexagons, see Fig. 3-1(a).

The anyons have the same statistical properties as $\nu = 1/3$ Laughlin quasi-particles: they pick up a phase of 2π when moved all the way around an electron (as can be seen from the Laughlin wavefunction). Since the electron density is $1/3$ per unit cell, this contributes a $2\pi/3$ flux when moving around a unit cell. The anyon lattice translation vectors thus triple, such that the resulting band structure contains three or six degenerate minima. This has a dramatic consequence for the anyon gas: as these degenerate minima have distinct momentum quantum numbers, our anyons are now of multiple species.

In Fig. 3-1(b) we illustrate an anyon hopping with such a flux configuration and the corresponding bandstructure (Fig. 3-1(c)): we see six minima which can be labelled with the index $I = 1, 2, .., 6$. Hence this anyon gas is characterized by six anyon species with statistical angles of $\theta = \pi/3$, and we can ask what groundstate it forms.

For anyons in the lowest band, we can describe them with a flux-attachment procedure [66, 67, 68] where composite fermions ψ_I (also six species) are attached to a statistical field a_μ such that the resulting particles have the appropriate $\theta = \pi/3$ statistics. Here only flux from the anyons are included, as the flux giving our underlying $\nu = 1/3$ state had been considered earlier, where it resulted in multiple degenerate minima for the anyon dispersion hence creating multiple anyon species.

The Lagrangian is

$$\begin{aligned}\mathcal{L} &= \frac{\tilde{\nu}}{4\pi} a_\mu \partial_\nu a_\lambda \epsilon^{\mu\nu\lambda} + i\psi_I^\dagger(\partial_0 + ia_0 - i\frac{e}{3}\delta A_0)\psi_I \\ &+ \frac{1}{2m}|(\partial_i + ia_i - i\frac{e}{3}\delta A_i)\psi_I|^2 + ... \end{aligned} \tag{3.1}$$

where δA_μ is the probe external electromagnetic field, $\tilde{\nu}$ a constant and m the anyon mass. The "..." denotes other terms that do not affect the discussion, e.g. the Maxwell term or the Coulomb repulsion between fermions.

Determining $\tilde{\nu}$ is easier within a hydrodynamic approach [69, 70], where the low-energy collective modes can be described by a particle current j^μ

$$\mathcal{L} = \frac{\tilde{\nu}}{4\pi} a_\mu \partial_\nu a_\lambda \epsilon^{\mu\nu\lambda} - (a_\mu - \frac{e}{3}A_\mu) j^\mu; \tag{3.2}$$

$$j^\mu = \sum_I j_I^\mu, \quad \text{and} \quad j_I^\mu = \frac{1}{2\pi}\partial_\nu \tilde{a}_{\lambda I}\epsilon^{\mu\nu\lambda} \tag{3.3}$$

since each fermion number current can be associated with a $U(1)$ gauge field. Introducing a particle that carries an a_μ unit charge gives the source term $a_0\delta(\mathbf{x} - \mathbf{x_0})$. Varying with respect to a_0, we find this term creates an excitation of charge $Q = -e/\tilde{\nu}$ and is associated with $1/\tilde{\nu}$ units of the a_μ flux [71]. Hence, interchanging two such excitations induces a phase

$$\pi \times (\text{number of } a_\mu\text{-flux quanta}) \times (a_\mu \text{ charge}) = \frac{\pi}{\tilde{\nu}}$$

There is also a phase π from the core statistics of the composite fermions, so these two contributions give the full statistical angle, i.e.

$$\frac{\pi}{\tilde{\nu}} - \pi = \theta \tag{3.4}$$

Since $\theta = \pi/3$, we obtain $\tilde{\nu} = 3/4$.

3.2.1 Mean-field treatment

Within this flux-attachment scheme, we can use a mean-field approximation where the statistical flux bound to the composite fermions is smeared to form a constant background field: $a_\mu = \bar{a}_\mu + \delta a_\mu$ where the flux density $\epsilon^{ij}\partial_i \bar{a}_j$ takes a constant average value b, and $\delta a_\mu = 0$.

In this approximation, our anyon gas problem becomes that of fermions in a constant magnetic field b. Their resulting ground state depends simply on their filling fraction, which we can calculate from Eq. 3.1 by varying a_0:

$$\sum_I \psi_I^\dagger \psi_I = \frac{\tilde{\nu}}{2\pi}\epsilon^{ij}\partial_i \bar{a}_j = \frac{\tilde{\nu} b}{2\pi} \tag{3.5}$$

The filling fraction as ratio of electron density $\sum_I \psi_I^\dagger \psi_I$ to magnetic field density b, is

$$2\pi \frac{\sum_I \psi_I^\dagger \psi_I}{b} = \tilde{\nu} = 3/4 \tag{3.6}$$

The constant $\tilde{\nu}$ in front of our Chern-Simons term has become the filling fraction of the composite fermions (as distinct from the filling fraction of our electron system $\nu = 1/3$).

What is the groundstate of a system with six fermion species at a combined filling fraction of 3/4? This would favor a multi-layer analog of the Laughlin state [72]:

$$\Psi(\{z_i\}) = \prod_{I<J,i,j} (z_i^I - z_j^J) \prod_{I,i<j}^{I=6} (z_i^I - z_j^I)^2 e^{-\sum |z_i|^2/4l_B^2}$$

where z_i^I is the coordinate of the ith electron in the Ith layer, and can be described by a 6×6 K-matrix with 3's along the diagonal and 1's on the off-diagonal entries.

Including this term in our theory (which we denote with $\tilde{K}$ for this composite

fermion K-matrix) and substituting Eq. 3.3 in Eq. 3.2, we obtain

$$\begin{aligned}\mathcal{L} &= \frac{\tilde{\nu}}{4\pi} a_\mu \partial_\nu a_\lambda \epsilon^{\mu\nu\lambda} - (a_\mu - \frac{e}{3}A_\mu)\sum_I \frac{1}{2\pi}\partial_\nu \tilde{a}_{\lambda I}\epsilon^{\mu\nu\lambda} \\ &+ \frac{\tilde{K}_{IJ}}{4\pi}\tilde{a}_{\mu I}\partial_\nu \tilde{a}_{\lambda J}\epsilon^{\mu\nu\lambda} \end{aligned} \tag{3.7}$$

3.2.2 Allowing gauge-field fluctuations

To this mean-field solution, we can now add fluctuations of the gauge-field, i.e. $\delta a_\mu \neq 0$. Further, as $\delta a_\mu = \sum_I \delta\tilde{a}_{\mu I}/\tilde{\nu}$ (as can be seen from varying a_μ), we can substitute this δa_μ gauge-field out. With these steps, the following additional terms due to fluctuations are obtained

$$\delta\mathcal{L} = (\tilde{K}_{IJ} - \frac{1}{\tilde{\nu}})\frac{1}{4\pi}\delta\tilde{a}_{\mu I}\partial_\nu \delta\tilde{a}_{\lambda J}\epsilon^{\mu\nu\lambda} \tag{3.8}$$

which we can denote with an effective 6×6 K-matrix:

$$\begin{aligned} K &= \tilde{K}_{IJ} - \frac{1}{\tilde{\nu}} = \begin{pmatrix} 3 & 1 & \cdots & 1 \\ 1 & 3 & \cdots & 1 \\ \vdots & \vdots & \ddots & \vdots \\ 1 & 1 & \cdots & 3 \end{pmatrix} - \frac{4}{3}\begin{pmatrix} 1 & 1 & \cdots & 1 \\ 1 & 1 & \cdots & 1 \\ \vdots & \vdots & \ddots & \vdots \\ 1 & 1 & \cdots & 1 \end{pmatrix} \\ &= U^\dagger K' U \end{aligned} \tag{3.9}$$

In the second line we diagonalize K to find one zero eigenvalue in K', signifying a gapless mode (since the Chern-Simons term vanishes leaving the Maxwell term only). This gapless mode is a density mode and all the other modes are gapped as the composite fermions remain in a quantum Hall state, i.e. the system has the same properties as a superfluid [73, 74]. This presence of this gapless mode can be understood heuristically from Fig. 3-2 (a): The fermion density and flux density co-fluctuate in always the same ratio such as to leave the filling fraction constant locally. Hence the mean-field FQH groundstate remains the true local solution everywhere, so this density fluctuation is a gapless mode while the other excitations remain gapped.

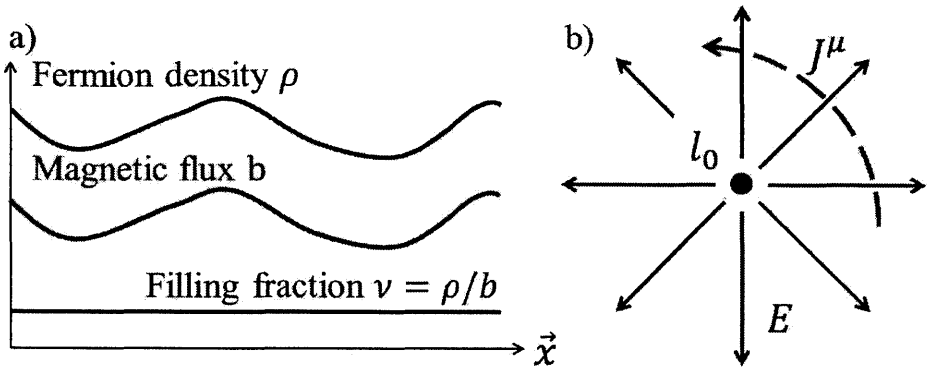

Figure 3-2: (a) Heuristic scheme of the superfluid gapless mode: As the fermion density fluctuates, so does the flux density since the flux-attachment scheme always combines fermions and flux in exactly the same ratio. Hence density fluctuations do not alter the ratio of fermion to flux density, leaving the filling fraction constant everywhere. This leaves the mean-field FQH groundstate of the composite fermions locally intact everywhere, so the density mode is a gapless excitation while the rest of the system remains gapped – forming a superfluid. (b) Vortex quantization of the superfluid current J_μ, created by the electric field E emanating from the charge l_0 in the dual picture.

3.3 Superfluid properties

We examine two aspects of the superfluid: the nature of the gapless mode, and gapped quasiparticle excitations.

For the former, this collective mode has a definite vortex quantization and can be calculated using 2+1 lattice duality (see Fig. 3-2 (b) and AppendixA.2 for details). We find the superfluid quantization is π/e, which corresponds to a superconducting quantization of $hc/2e$ – reminiscent of a BCS-like electron pair. However, without identifying an order parameter within this approach, we cannot conclude that a similar pairing mechanism occurs here, especially when the following discussion reveals clearly non-BCS-like properties as well.

We proceed to analyze properties of the gapped quasiparticles, i.e. excitations composed only of gauge-fields with a finite Chern-Simons term and hence short-

ranged interactions. Such excitations are described by a vector orthogonal to the zero-mode eigenvector (of the K-matrix in Eq. 3.9); further its entries are integers for quantized excitations ($\boldsymbol{l}$-vectors) [71].

The set of such possible vectors fall in two kinds: $\boldsymbol{l}$-vectors that contain fractionalized statistics and those with trivial statistics. The former describe non-local excitations while the latter are simply bound states of electrons (bosons and fermions). We would like to identify all different types of non-local excitations; after all, if a non-local excitation is merely a composite of another non-local excitation and a trivial excitation – these two excitations have the same fractional statistics and can be considered the same type.

We find 15 non-trivial particles with mutual semion statistics, which can be generated with the following four-vector basis of $\{l_{\alpha\beta\gamma\delta}\}$-vectors (where $\alpha, \beta, \gamma, \delta = \{0, 1\}$ only)

$$\begin{aligned} \boldsymbol{l}_{1000} &= (1,0,-1,0,0,0)^T, \\ \boldsymbol{l}_{0100} &= (0,0,1,-1,0,0)^T, \\ \boldsymbol{l}_{0010} &= (1,0,0,0,-1,0)^T, \\ \boldsymbol{l}_{0001} &= (0,1,0,-1,0,0)^T. \end{aligned} \tag{3.10}$$

Composites of two identical particles are trivial, so each of the four indices take only 0 or 1 to be actually different excitations (there is a $\mathbb{Z}_2$ fusion structure for each, separately). However, a composite of two different particles, e.g. $\boldsymbol{l}_{1100} = \boldsymbol{l}_{1000} + \boldsymbol{l}_{0100}$ is another non-trivial excitation distinct from the underlying two, giving rise to $2^4 = 16$ possible combinations in total ($\boldsymbol{l}_{0000}$ is trivial and the other 15 are not). Hence the fusion relations between these particles have a group structure of $(\mathbb{Z}_2)^4$.

Each $\boldsymbol{l}$-vector is a 6-component integer vector where each component refers to the composite fermion species I. The statistics of these excitations can be calculated using $l_a^T K_{\text{eff}}^{-1} l_b$ where K_{eff}^{-1} is a 6×6 matrix obtained from K in Eq. 3.9. In the diagonal basis of K' and U, we can identify the zero-mode subspace and remove it,

leaving a 5×5 K'_{eff} and a 5×6 U_{eff}. This allows the inversion of K'_{eff} and we obtain

$$K_{\text{eff}}^{-1} = U_{\text{eff}}^{\dagger} K'_{\text{eff}} U_{\text{eff}}, \tag{3.11}$$

a 6×6 matrix which here has 5/12 all along the diagonal and -1/12 for all off-diagonal entries.

Intrinsic topological order — We illustrate the modular matrix $S_{ab} = \frac{1}{\sqrt{D}} \exp(2\pi l_a^T K_{\text{eff}}^{-1} l_b)$ (D is the quantum dimension for normalization [75]) for just the four generating vectors listed in Eq. 3.10:

$$S = \frac{1}{4} \begin{pmatrix} 1 & -1 & -1 & 1 \\ -1 & 1 & 1 & -1 \\ -1 & 1 & 1 & 1 \\ 1 & -1 & 1 & 1 \end{pmatrix} \tag{3.12}$$

where the -1 entries are the mutual semion statistics.

The matrix S for all 16 quasiparticle types can be calculated, along with the diagonal twist matrix $T = \delta_{ab} \exp(\pi l_a^T K_{\text{eff}}^{-1} l_b)$. We find that these matrices satisfy the modular group relations as expected for a bosonic topological order, e.g.

$$(ST)^3 = \exp \frac{\pi i c}{4} S^2 \tag{3.13}$$

where the central charge c here is 4.

3.4 Other possible scenarios

Our method depends upon particular choices of parameters and this previous example is just one choice. Here we examine other possible outcomes within this scheme. For instance, the statistical angle of Laughlin quasiparticles could be $-\pi/3$ instead of $\pi/3$, which would modify the result obtained from Eq. 3.4 to give $\tilde{\nu} = 3/2$ instead. In this case, our six composite fermions would have a combined filling fraction of 3/2,

where a favourable groundstate could be three Halperin states each at filling fraction 1/2.

The Halperin wavefunction is expected to be the groundstate of a bilayer system at filling fraction 1/2 [72]:

$$\Psi_H(\{z_i\}) = \prod_{I<J,i,j} (z_i^I - z_j^J) \prod_{I,i<j}^{I=2} (z_i^I - z_j^I)^3 e^{-\sum |z_i|^2/4l_B^2}$$

when the intra-layer repulsion is stronger than the inter-layer repulsion. The K-matrix is three copies of the K-matrix for a bilayer system:

$$K_H = \begin{pmatrix} 3 & 1 \\ 1 & 3 \end{pmatrix}, \quad \tilde{K} = \begin{pmatrix} K_H & 0 & 0 \\ 0 & K_H & 0 \\ 0 & 0 & K_H \end{pmatrix}$$

Repeating a similar analysis, we find once again a zero-mode with the same superfluid vortex quantization. The possible gapped quasiparticles are now generated by just two $\{l_{\alpha\beta}\}$-vectors

$$\begin{aligned} \boldsymbol{l}_{10} &= (0,1,-1,0,0,0)^T, \\ \boldsymbol{l}_{01} &= (-1,0,2,0,0,-1)^T. \end{aligned} \tag{3.14}$$

but now $\alpha, \beta = \{0, 1, ..., 7\}$, i.e. each excitation has a separate fusion structure of $\mathbb{Z}_8$. Together, they form $8^2 = 64$ possible combinations and have a combined fusion structure of $(\mathbb{Z}_8)^2$.

As above, we can compute their mutual statistics using the appropriate K_{eff}^{-1}, which here has $1/3$ along the diagonal, $-1/6$ on off-diagonal entries within each bilayer and $-1/24$ on all remaining off-diagonal entries. Again we present the S matrix for the two generating vectors in Eq. 3.14:

$$S = \frac{1}{8} \begin{pmatrix} -i & \exp\frac{3i\pi}{4} \\ \exp\frac{3i\pi}{4} & i \end{pmatrix} \tag{3.15}$$

Besides the strangeness of the statistics obtained, we find the relation in Eq. 3.13 is violated as $(ST)^3 = -\mathbb{I}$ whereas S^2 is an off-diagonal matrix (while $S^4 = \mathbb{I}$). Hence this is not a bosonic topological order, and it is unclear if this topological order that comes with a gapless mode has the same properties as topological order of a fully gapped system.

3.5 BCS-like state

The last possible scenario we present is a case with particularly simple results, with properties similar to that obtained from BCS theory. If the anyon hopping is frustrated, this adds a minus sign to all the anyon hoppings in Fig. 3-1(b) and the lowest band becomes the flipped version of Fig. 3-1(c). What were previously three maxima become the location of three minima, which results in just three composite fermion species instead of six.

Considering the filling fraction $\tilde{\nu} = 3/2$, we see that if all three fermions have the same density, they each have a filling fraction of $1/2$, which is a compressible state.

However, if the lattice translation symmetry is broken by spontaneous formation of a charge-density wave or by the application of a periodic electrostatic potential, this could suppress some of the fermion species density relative to others. Here we choose to work in an alternate Wannier basis where the index I for fermion species now denotes fermion species in real and not momentum space [76].

With a charge imbalance where two species have a relative density of $1/4$ compared to the third (see Fig. 3-3), this would be a Halperin state for the first two species and an integer quantum Hall state for the last. This is described by the K-matrix

$$\tilde{K} = \begin{pmatrix} K_H & 0 \\ 0 & 1 \end{pmatrix}$$

and has a zero mode with the same $2e$ quantization like in previous examples, with quasiparticle excitations that are non-fractionalized.

These purely local quasiparticle excitations can be described with the $\boldsymbol{l}$-vectors

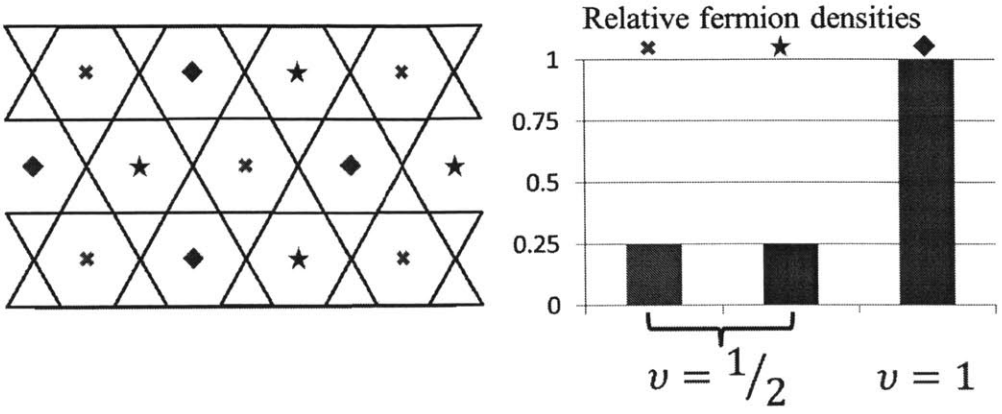

Figure 3-3: (a)Breaking of translation symmetry in the lattice, where the three species (cross, star and diamond) have different relative densities. This could happen by spontaneous formation of a charge-density wave or by the application of a periodic electrostatic potential. (b) When the first two species have a relative density of 1/4 compared to the third, this favors a Halperin state for the first two species and an integer quantum Hall state for the third.

and topologically trivial S matrix

$$\begin{aligned} \boldsymbol{l}_1 &= (-2,-2,1)^T, \quad \boldsymbol{l}_2 = (-1,1,0)^T; \\ S &= \frac{1}{\sqrt{2}} \begin{pmatrix} 1 & 1 \\ 1 & 1 \end{pmatrix}. \end{aligned} \tag{3.16}$$

3.6 Discussion

We show that flat band systems which support a FQH state at commensurate filling, could support a superfluid mode at incommensurate filling. Such a state may have intrinsic topological order, and we present one example of bosonic topological order with anyon fusion statistics of $(\mathbb{Z}_4)^2$ and a second non-bosonic topological order with fusion statistics of $(\mathbb{Z}_8)^2$. Another possible outcome is a state similar to that from BCS theory, which suggests that such a state could also be described using more direct methods like mean-field theory.

While our model has been based on a kagome lattice, our results essentially rest on the effects of an underlying lattice where the FQH state can be realized. A different

route to the same physics is through application of a periodic potential in other continuum-like FQH systems, including semiconductors or graphene.

In order to identify which groundstate has the lowest energy, further work is needed. Besides numerical simulations, the results here suggest anyon wavefunctions and more indirectly, electron wavefunctions, that can be useful in suggesting compatible Hamiltonians or appropriate variational wave-functions. Another open question is what chiral edge modes this superfluid contains, and how they combine with the edge mode from the underlying electron $\nu = 1/3$ state.

Chapter 4

Strain-induced partially flat band, helical snake states, and interface superconductivity in topological crystalline insulators

Topological crystalline insulators in IV-VI compounds host novel topological surface states consisting of multi-valley massless Dirac fermions at low energy. Here we show that strain generically acts as an effective gauge field on these Dirac fermions and creates pseudo-Landau orbitals without breaking time-reversal symmetry. We predict the realization of this phenomenon in IV-VI semiconductor heterostructures, due to a naturally occurring misfit dislocation array at the interface that produces a periodically varying strain field. Remarkably, the zero-energy Landau orbitals form a flat band in the vicinity of the Dirac point, and coexist with a network of snake states at higher energy. We propose that the high density of states of this flat band gives rise to interface superconductivity observed in IV-VI semiconductor multilayers at unusually high temperatures, with non-BCS behavior. Our work demonstrates a new route to altering macroscopic electronic properties to achieve a partially flat band, and paves the way for realizing novel correlated states of matter.

4.1 TCIs and their surface states

The recently discovered topological crystalline insulators host novel topological surface states that are protected by the symmetry of the underlying crystal[26, 27, 28, 29]. At low carrier energy, these surface states consist of multi-valley massless Dirac fermions, whose characteristic properties are highly tunable by external perturbations. Breaking the crystal symmetry at the atomic scale generates a Dirac mass and leads to gapped phases[26, 30] with potentially novel functionalities in low-power electronics and spintronics[31, 32, 33].

The (001) surface states of topological crystalline insulators SnTe and $Pb_{1-x}Sn_xTe(Se)$ consist of massless Dirac fermions at four valleys that exhibit spin texture of the same chirality[26]. The four Dirac points are located at two pairs of opposite momenta, denoted by $\pm\mathbf{K}_1$ and $\pm\mathbf{K}_2$, in the vicinity of the X_1 and X_2 point in the surface Brillouin zone respectively. $\mathbf{K}_1$ and $\mathbf{K}_2$ are related by four-fold rotation around the surface normal, while $+\mathbf{K}_j$ and $-\mathbf{K}_j$ are related by time-reversal symmetry (see Fig.1a). Importantly, unlike in the case of topological insulators[25, 77, 78], the Dirac points in topological crystalline insulators are not pinned at time-reversal-invariant momenta[79], because their massless nature is protected by crystal symmetry instead of time reversal[80, 81]. As a consequence, perturbations can move such Dirac points in momentum space, mimicking the effect of a gauge field vector potential without breaking time reversal symmetry. Two effective ways of moving surface Dirac points in topological crystalline insulators are (i) alloy composition tuning, as recently demonstrated in $Pb_{1-x}Sn_xTe(Se)$[82] and (ii) strain, which is the subject of this work.

We first use symmetry analysis to determine the general form of strain-induced Dirac point displacement on the topological crystalline insulator (001) surface, which is equivalent to a strain-induced gauge field vector potential $\mathbf{A}_j \equiv \mathbf{K}'_j - \mathbf{K}_j$ acting on the Dirac fermion at valley $\mathbf{K}_j$. To lowest order, $\mathbf{A}_j = (A_j^x, A_j^y)$ is linearly proportional

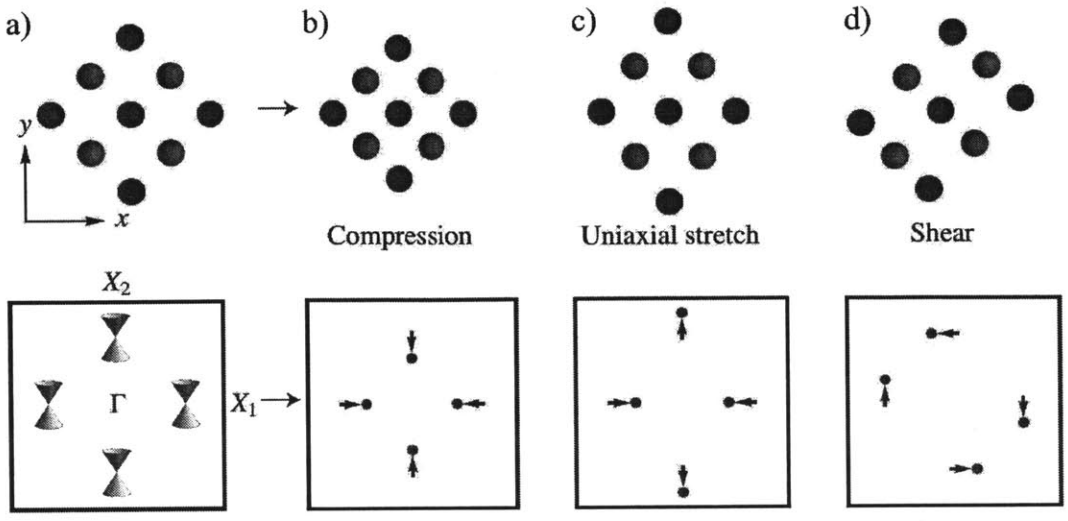

Figure 4-1: Strain-induced Dirac point shift on the (001) surface of a topological crystalline insulator such as SnTe and $Pb_{1-x}Sn_xSe(Te)$. Top: strain on the rocksalt structure of a) compression, b) uniaxial stretch and c) shear; the x and y axes are in the (110) and $(1\bar{1}0)$ directions respectively. Bottom: the corresponding strain-induced shift (arrows) of Dirac points to new positions (circles) in the (001) surface Brillouin zone, which is equivalent to an effective gauge field.

to the strain field u_{ij} as given by (see Appendix B):

$$\begin{aligned} \mathbf{A}_1 &= (\alpha_1 u_{xx} + \alpha_2 u_{yy},\ \alpha_3 u_{xy}), \\ \mathbf{A}_2 &= (\alpha_3 u_{xy},\ \alpha_1 u_{yy} + \alpha_2 u_{xx}). \end{aligned} \tag{4.1}$$

where $u_{ij} \equiv (\partial_j u_i + \partial_i u_j)/2$ is the spatial gradient of the displacement field $\mathbf{u}$, and the coordinate axes x and y are along the [110] and $[\bar{1}10]$ directions respectively. α_1, α_2 and α_3 denote three independent coupling constants.

4.2 Strain acts as a gauge-potential

As shown in Fig.1, under a given type of strain, the Dirac fermions at valleys $\mathbf{K}_1$ and $\mathbf{K}_2$ experience distinct gauge fields $\mathbf{A}_1$ and $\mathbf{A}_2$. In addition, opposite gauge fields $-\mathbf{A}_j$ are induced at the Dirac valleys $-\mathbf{K}_j$ as required by time reversal symmetry.

A uniform strain can only produce a constant gauge field vector potential, which

yields zero pseudo-magnetic field $\mathbf{B} \equiv \nabla \times \mathbf{A}$. Instead, a highly inhomogeneous strain is required to create a strong pseudo-magnetic field, which is difficult to engineer with high precision and control. Such a field was previously observed in graphene nanobubbles[83, 84, 85, 86], which are however localized within nanoscale regions thus leaving electronic properties on a large scale essentially unaltered.

Here we show that a periodic pseudo-magnetic field covering macroscopic spatial regions arises naturally in IV-VI semiconductor (001) heterostructures consisting of a topological crystalline insulator and a trivial insulator. This field is created by misfit dislocations that are known to spontaneously form at the interface due to lattice mismatch. Remarkably, these dislocations self-organize into a nearly perfect two-dimensional square array with a period of 3-25nm (see Fig.2), as observed by transmission electron spectroscopy, X-ray diffraction, and scanning tunneling microscopy in SnTe/PbTe, PbTe/PbS, PbTe/PbSe, and PbTe/YbS[87, 88, 89]. This dislocation superstructure naturally produces an inhomogeneous strain field, which gives rise to an unusual pseudo-magnetic field $\mathbf{B}(x, y)$ that alternates with a nanoscale period and averages to zero. Instead, it should be pointed out that the widely studied uniform pseudo-magnetic field is physically impossible in the thermodynamic limit, due to the bounded nature of strain.

To calculate $\mathbf{B}(x, y)$, we first note the experimental observation[89] that the dislocation array is a superposition of two sets of equally spaced parallel dislocation lines along the x and y directions respectively. Each line is an edge dislocation with a Burgers vector $\mathbf{b} = \frac{a}{2}\hat{z} \times \hat{e}$ (a is the lattice constant), which is parallel to the interface and perpendicular to the line direction $\hat{e} = \hat{x}$ or $\hat{y}$. The set of dislocation lines along the y direction creates a displacement field at the interface. The corresponding strain field contains two in-plane components u_{xx} and u_{yy} that periodically vary in the x direction. u_{xx} and u_{yy} are the sum of strains from each dislocation line indexed by

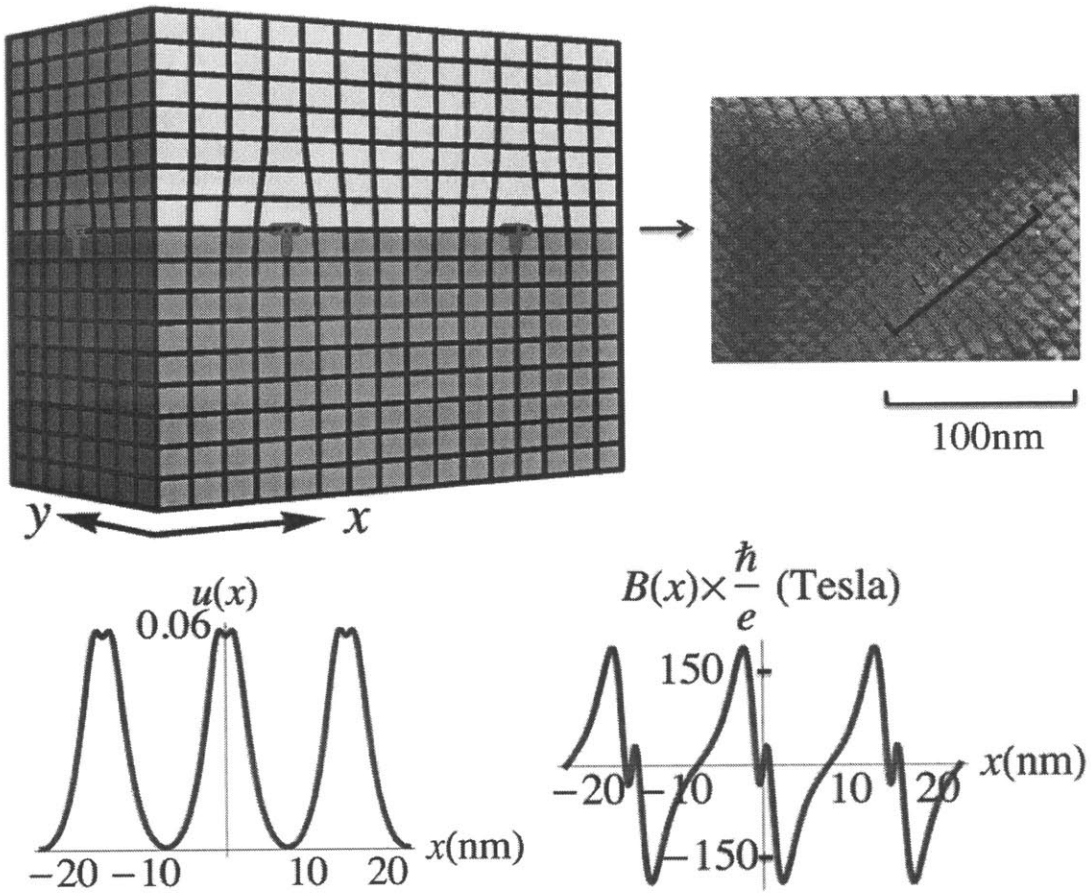

Figure 4-2: The spontaneous formation of a misfit dislocation array gives rise to a periodically varying strain field and pseudo-magnetic field, at the interface. Top: a square array of misfit edge dislocations is spontaneously formed at the (001) interface of two IV-VI semiconductors (e.g., PbTe/PbSe), due to lattice mismatch. The array consists of dislocation lines along both x and y directions, as shown in the transmission electron microscopy image taken from Ref.[4]. Bottom: the set of dislocation lines along the y direction creates a periodically varying strain field $u(x) \equiv u_{xx}(x) + u_{yy}(x)$ as a function of x given by Eq.(4.3). This is plotted here using the realistic parameters: $\lambda = 15$nm, $z = 2$nm, $\nu = 0.26$ and $a = 6.4$ (see main text), together with the pseudo-magnetic field $B(x)$ it generates.

N:

$$\begin{aligned} u_{xx}(x) &= \sum_N u^0_{xx}(x - N\lambda), \\ u_{yy}(x) &= \sum_N u^0_{yy}(x - N\lambda), \end{aligned} \tag{4.2}$$

where λ is the dislocation array period. Within linear elasticity theory, u^0_{xx} and u^0_{yy} are given by[90]

$$\begin{aligned} u^0_{xx}(x) &= \frac{bz}{2\pi(1-\nu)} \frac{(3x^2+z^2)}{(x^2+z^2)^2}, \\ u^0_{yy}(x) &= \frac{bz\nu}{\pi(1-\nu)} \frac{1}{x^2+z^2}. \end{aligned} \tag{4.3}$$

Here z is the distance from the dislocation plane, ν is the Poisson's ratio and b is the magnitude of the Burger's vector $\mathbf{b}$. Similarly, the set of dislocation lines along the x direction creates strain fields $\tilde{u}_{xx}$ and $\tilde{u}_{yy}$, which are related to u_{xx} and u_{yy} by the $\pi/2$ rotation: $\tilde{u}_{xx}(y) = u_{yy}(x \to y)$ and $\tilde{u}_{yy}(y) = u_{xx}(x \to y)$.

The total strain fields $u_{xx}(x) + \tilde{u}_{xx}(y)$ and $u_{yy}(x) + \tilde{u}_{yy}(y)$ create gauge fields for the two-dimensional Dirac fermions at the interface. It follows from Eq.(4.1) that the gauge field $\mathbf{A}_j$ for the Dirac fermion at $\mathbf{K}_j$ contains both longitudinal and transverse components, $\mathbf{A}_j = \mathbf{A}^L_j + \mathbf{A}^T_j$. The longitudinal component $\mathbf{A}^L_j$ can be "gauged away" by a unitary transformation hence will not be considered below. The transverse component $\mathbf{A}^T_j$ is given by

$$\begin{aligned} \mathbf{A}^T_1(y) &= (\alpha_1 \tilde{u}_{xx}(y) + \alpha_2 \tilde{u}_{yy}(y), 0), \\ \mathbf{A}^T_2(x) &= (0, \alpha_1 u_{yy}(x) + \alpha_2 u_{xx}(x)), \end{aligned} \tag{4.4}$$

which yields an out-of-plane pseudo-magnetic field B_j acting on the Dirac fermion at valley $\mathbf{K}_j$: $B_1(y) = \nabla \times \mathbf{A}^T_1(y)$ and $B_2(x) = \nabla \times \mathbf{A}^T_2(x)$. Note that although the dislocation array is two-dimensional, the pseudo-magnetic field for a given Dirac valley is periodically alternating in one direction only.

We now estimate the magnitude of the pseudo-magnetic field created by misfit

dislocation arrays at the interface. For a typical array period of $\lambda = 15$nm at $z = 2$nm, with the Poisson ratio for PbTe of $\nu = 0.26$[91] and the lattice constant $a = 6.4$, the corresponding strain field $u = u_{xx} + u_{yy}$, plotted in Fig.4-2, has a maximum value of 6%, which is comparable to the $3 - 10\%$ lattice mismatch in IV-VI semiconductor heterostructures[87, 88, 89]. A recent ab-initio calculation[92] finds that the Dirac point positions of strained PbTe in the topological crystalline insulator phase shift linearly under compression, and yields $\alpha_1 = 2.2^{-1}$. Assuming $\alpha_2 \approx \alpha_1 \equiv \alpha$, we find a Dirac point displacement of $A_0 = 0.13^{-1}$ under the maximum 6% strain, which is comparable to the displacement under changes in alloy composition in $Pb_{1-x}Sn_xTe$ as recently observed by angle-resolved photoemission spectroscopy[82]. Using this value of α, we plot the periodically alternating pseudo-magnetic field created by the dislocation array in Fig.4-2. The maximum field strength is around 180T.

4.3 Spatially-varying psuedo magnetic field: Landau levels

How does this pseudo-magnetic field change the electronic structure of Dirac fermion surface states at the interface? We first analyze this problem using a local field approximation. When the magnetic field is uniform, two-dimensional massless Dirac fermions form a set of Landau levels. In the Landau gauge, the Landau orbitals are one-dimensional strips localized at different x positions and infinite in the y direction. The width of the strip is set by the magnetic length $L_B = 1/\sqrt{|B|}$. When the magnetic field $B(x)$ is slowly varying over the distance L_B, the Landau level strip remains an approximate energy eigenstate. However, the Landau level energy becomes position dependent and is determined by the local magnetic field:

$$E_n(x) = \mathrm{sgn}(n)\sqrt{2nv_xv_y|B(x)|}. \tag{4.5}$$

where $v_x(v_y)$ is the Dirac fermion velocity in the $x(y)$ direction. Since the x position of a Landau level strip is proportional to its momentum in the y direction i.e. $x \propto$

$\mathrm{sgn}(B)k_y$, the Landau level energy $E_n(x)$ as a function of position x is also the dispersion as a function of momentum k_y. Thus, when the magnetic field is spatially varying, Landau levels at different positions become non-degenerate and collectively form a *dispersive* band. It should be clear from this analysis that the extensive degeneracy at $E = 0$ holds so long as the strain field varies slowly over L_B even without being strictly periodic.

The $n = 0$ Landau level of massless Dirac fermions deserves special attention. Its energy is pinned at $E_0 = 0$ independent of the magnetic field strength, as recently observed in topological crystalline insulators[30]. This implies that in a slowly varying pseudo-magnetic field, the $n = 0$ Landau orbitals remain extensively degenerate at zero energy, forming a flat band.

To demonstrate this, we numerically calculate the energy spectrum of massless Dirac fermions under the periodically alternating pseudo-magnetic field created by the dislocation array. The Hamiltonian is given by

$$H = -iv_x\partial_x s_y - v_y(k_y - A_y(x))s_x, \tag{4.6}$$

where s_x and s_y are Pauli matrices. Here we have chosen to study the Dirac valley $\mathbf{K}_2$, for which the strain-induced gauge field $A_y(x)$ is given in Eq.(4.4). For simplicity, we approximate the strain field shown in Fig.4-2 as a cosine function in our calculation, i.e., $A_y(x) = A_0\cos(2\pi x/\lambda)$. The main findings presented below are independent of the specific choice of $A_y(x)$.

It is instructive to express H in terms of the dimensionless quantities $\tilde{x} \equiv x/\lambda$, $\tilde{y} \equiv v_x y/v_y\lambda$ and $\tilde{H} \equiv \lambda H/v_x$:

$$\tilde{H} = -i\partial_{\tilde{x}} s_y - (\tilde{k}_y - \beta\cos(2\pi\tilde{x}))s_x. \tag{4.7}$$

The energy spectrum of $\tilde{H}$ is entirely determined by a single dimensionless parameter $\beta = (v_y/v_x)A_0\lambda \propto \sqrt{\lambda/L_B}$, which depends on the ratio of the dislocation array period and the magnetic length. The formation of local Landau levels and flat bands requires $\beta \gg 1$. To estimate the realistic value of β, we use the aforementioned

parameter $A_0 = 0.13^{-1}$, and take Dirac velocities from an ab-initio calculation[79]: $v_x = 0.84eV, v_y = 1.3eV$. This yields $\beta \approx 20 - 40$ for $\lambda = 10 - 20$nm, fulfilling the condition for flat bands.

4.4 Partially flat bands and snake states

A representative band structure of H for $\beta = 30$ is plotted in Fig. 4-3a. As expected, we find two bands become very flat at zero energy for $|k_y| < k_c = 0.05^{-1}$. These two degenerate flat bands correspond to two types of $n = 0$ Landau level strips that reside in different spatial regions under positive and negative pseudo-magnetic fields respectively. The x position of Landau level strips in $B > 0$ ($B < 0$) regions increases (decreases) linearly with k_y. For $|k_y| > k_c$, these two types of Landau levels become hybridized in "transition regions" where B goes through zero, which are centered either on a dislocation line at $x = N\lambda$ or at the midpoint $x = (N + \frac{1}{2})\lambda$ between adjacent dislocations. As a consequence of the level splitting from hybridization, the two zero-energy flat bands at $|k_y| < k_c$ evolve into a pair of dispersive bands at $|k_y| > k_c$, which reside on the domain wall between $n = 0$ Landau levels under positive and negative pseudo-magnetic fields (see Fig. 4-3b).

These dispersive states have a topological origin related to the unique half-integer Hall conductance of the $n = 0$ Landau level of a single massless Dirac fermion: $\sigma_{xy} = \mathrm{sgn}(\mu B)\frac{1}{2}\frac{e^2}{h}$, where μ is the chemical potential. Because Hall conductances in $B > 0$ and $B < 0$ regions differ by $\Delta\sigma_{xy} = \mathrm{sgn}(\mu)e^2/h$, there exists one branch of chiral snake states at the domain wall[93], which is derived from the valley $\mathbf{K}_2$ and moves parallel to the y axes. The existence of these snake states, which is required by topology, leads to the electron-hole symmetric dispersion at large k_y shown in Fig. 4-3a. The opposite velocities of snake states at $\mu > 0$ and $\mu < 0$ are required by the sign reversal of σ_{xy}.

The above topological flat bands and snake states derived from the Dirac valley at $\mathbf{K}_2$ have a time-reversed partner from the opposite valley at $-\mathbf{K}_2$ with opposite spin polarizations, as well as $\pi/2$-rotated copies from the two other valleys at $\pm\mathbf{K}_1$. Taking

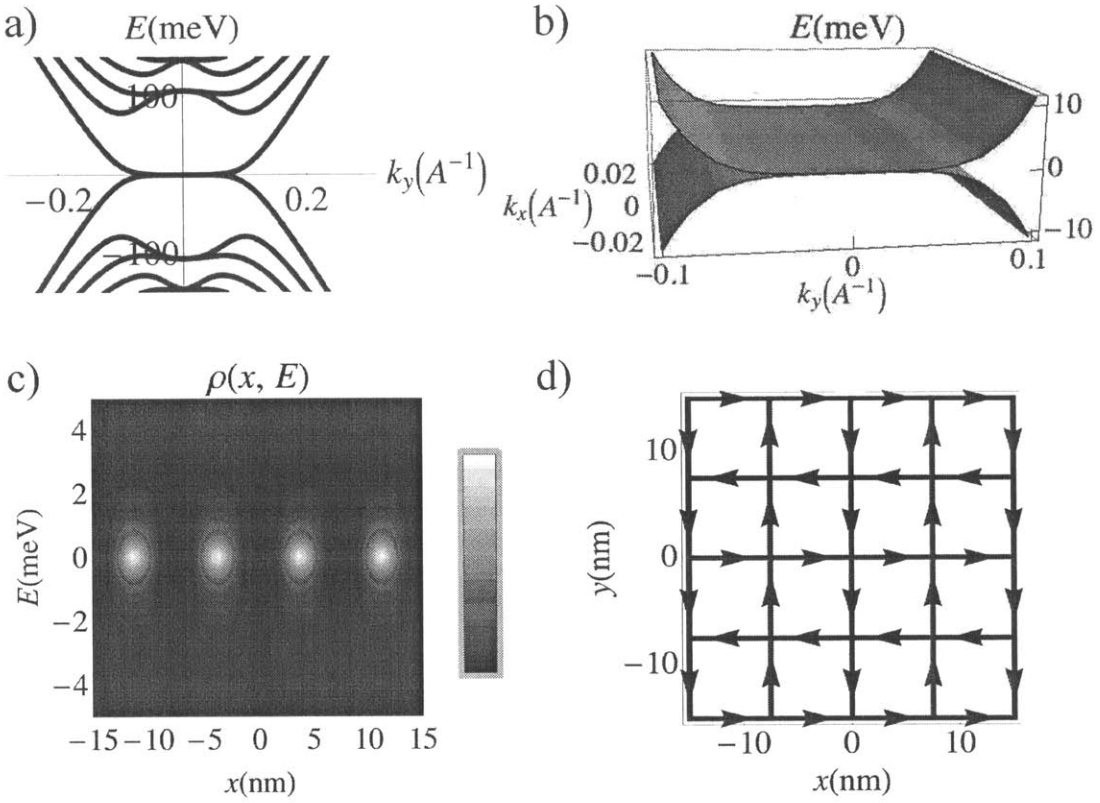

Figure 4-3: The pseudo-magnetic field from strain creates flat bands and snake states. (a) Under a periodically alternating pseudo-magnetic field $B(x)$, the initially linear Dirac dispersion becomes flat within a finite range of k_y in the vicinity of the Dirac point, while higher Landau levels are more dispersive. (b) The band is completely flat in k_x, which has a much reduced period given by the dislocation superlattice Brillouin zone. (c) Local density of states $\rho(x, E)$ as a function of position x and energy E, showing zero-energy Landau levels from regions of both positive and negative pseudo-magnetic field, which are spatially separated by dispersive snake states. (d) One-dimensional snake states appear where the pseudo-magnetic field changes sign. This schematic cartoon shows snake states from valleys $\mathbf{K}_1$ and $\mathbf{K}_2$ moving along the y and x directions respectively, which form a two-dimensional network. Please refer to the main text for parameters used.

all four valleys into account, we conclude that the dislocation array causes dramatic band reconstruction on the (001) surface by creating flat dispersions in the vicinity of the Dirac points and a two-dimensional network of helical snake states at higher energy. Due to the helical nature of topological surface states, counter-propagating snake states on the same domain wall cannot backscatter, and the two-dimensional surface of topological crystalline insulators remains conducting even in the presence of disorder[94], unlike non-topological flat bands that are prone to Anderson localization.

Recently flat-band systems have attracted tremendous interest due to enhanced interaction effects associated with the high density of states and the resulting electronic instabilities. Most studies have focused on finding a completely flat band with nontrivial topology, which appears to rely on careful fine tuning of material parameters and has not been experimentally realized so far. In comparison, our work reveals a new and realistic route to achieve a partially flat band, as shown in Fig.3. For a wide range of electron or hole densities (up to about $5 \times 10^{12}\text{cm}^{-2}$ in this example), the Fermi energy lies within the partially filled flat band. It is thus natural to ask whether interesting interaction-driven phenomena are expected to arise.

4.5 Comparison with measured interface superconducitivity

In this regard, we note that a wide class of IV-VI semiconductor (001) multilayers and bilayers is superconducting. Superconductivity was first discovered in PbTe/SnTe, PbSe/PbS, PbTe/PbSe, PbS/YbS and PbTe/YbS superlattices long ago[95, 96, 97], and recently found in two-layer sandwiches of PbTe/PbS, PbTe/PbSe, and PbTe/YbS with layers 40–300nm thick[98, 99]. The transition temperatures T_c are in the range of 2.5–6.4K, which is unusually high for semiconductors especially given that the individual constituent materials are non-superconducting (the only exception is SnTe with the very low T_c of 0.22K). Further, the strong anisotropy of the upper critical field reveals that the observed superconductivity is two-dimensional[98, 99]. Based on

these facts, it was concluded that the locus of superconductivity is at the interface.

Remarkably, it was found that the appearance of superconductivity is dependent on the formation of a misfit dislocation array near the interface[4, 100]. Samples with island-type growth, and therefore dislocations that do not cover the whole interface only show partial superconducting transitions. For superconducting samples, the transition temperature T_c was found to increase from 3K to 6K as the period of the misfit dislocation array λ decreases from 23nm to 10nm[4].

Previous works[97, 4] have proposed that superconductivity emerges from metallic interface states created by band inversion on one side of the interface where the constituent material is pseudomorphic and in compression. Such band inversion due to compression is only possible for narrow-gap semiconductors, which explains the absence of superconductivity down to 1.5K in IV-VI multilayers consisting of only wide-gap semiconductors (YbS/EuS, YbS/YbSe). However, this proposal does not take into account the indispensable role of dislocations in superconductivity, nor explain the origin of the unusually high transition temperature.

Our work sheds new light on the interface superconductivity in IV-VI multilayers. The band inversion induced by compression leads to the topological crystalline insulator phase[26], and hence gives rise to topological surface states at the interface whose electronic properties were correctly identified only recently[26, 27, 29, 28, 79]. At the same time, the dislocation array produces a periodically varying strain, which acts on these states to create topological flat bands. In the presence of attractive interaction due to electron-phonon coupling, the high density of states associated with these flat bands dramatically increases the superconducting transition temperature.

Our proposal of interface superconductivity from dislocation-induced flat bands provides a remarkable explanation of the unusual dependence of T_c on the dislocation array period[4]. As shown recently, the superconducting transition temperature T_c in a flat-band system is linearly proportional to the area of the flat band in momentum space[101, 102], which is *parametrically* enhanced compared to BCS theory. In our proposal, when the distance between dislocation lines is large, the pseudo-magnetic field created by the strain field (4.3) is largely concentrated around individual dis-

location lines, thus the zero-energy Landau orbitals from different dislocations are spatially separated. In this regime, the area of the flat bands in momentum space is proportional to the reciprocal superlattice vector $2\pi/\lambda$, and thus T_c increases with decreasing array period. When λ becomes too small, however, Landau orbitals start to overlap and band flatness gets destroyed, hence T_c stops increasing. In effect, the dependence of T_c on the flat band degeneracy results in its non-monotonic dependence on the array period, in agreement with the experimental observation[4].

We further predict two testable signatures of flat bands in topological crystalline insulators and their prominent role in interface superconductivity in IV-VI semiconductor multilayers. First, the flat bands and coexisting network of helical snake states generate a distinctive local density of states spectrum as a function of position and energy shown in Fig.3c, which can be detected in tunneling (magneto-)conductance measurements[103], de Haas-van Alphen or Shubnikov-de Haas oscillations. Second, the enhancement of superconductivity by flat bands ceases to work when the flat bands become empty or filled. This leads to a drop in T_c as the carrier density at the interface increases above a threshold, whose value depends on the strain field strength and dislocation array period and is estimated to be on the order of 10^{12}cm^{-2}.

While the superconducting transition temperatures in IV-VI heterostructures are not high on an absolute scale, the mechanism of flat band formation due to interface microstructures or intentional strain engineering may offer a viable route to high-temperature interface superconductivity—a subject of tremendous current interest[104, 105]. Further, our work opens up new directions for achieving other interesting phases in a realistic setting. In particular, when interactions are repulsive[106, 107, 108], novel quantum Hall states or fractional topological insulators may arise in the helical flat band we have found, at zero magnetic field. While electron repulsion is weak in IV-VI semiconductors due to their large dielectric constants, new topological crystalline insulator materials have recently been predicted/proposed in correlated electron systems such as heavy fermion compounds[109, 110], transition metal oxides[111], graphene multilayers[112] and anti-perovskites[113]. These rapid and continuing developments hold promise for the physical realization of new states

of matter in partially flat bands.

Chapter 5

Superconducting interaction in a flat band

In this chapter we re-examine the question of how the superconducting interaction dominates the Coulomb repulsion to result in an effective attractive interaction for superconductivity to occur. While this issue has been solved for a typical electron gas with a large bandwidth, that criteria appears to break down for a flat band. Our results in the previous chapter or other experiments in interface superconductivity prompt the re-examination of this question in the flat band context.

A solution was first suggested by Anderson and Morel in 1962 [114] where they demonstrated that even while the phonon energy scale (Debye energy ϵ_D) is much smaller than the electronic Coloumb scale, the more rapid electron time scale allows for renormalization of the repulsive interaction to give an effectively attractive interaction overall (retardation effect). We review their calcuation in the first section below. Their calculation assumes a constant density of states, which is appropriate for a usual Fermi surface around the Fermi energy.

In a flat band however, the density of states of sharply peaks at the flat band energy and drops off outside that window, i.e. the flatband bandwidth $\Gamma_{FB} \ll \epsilon_D$. In this case, it is questionable whether the Coloumb repulsion can still be renormalized, as it is typically when the electron bandwidth $W \gg \epsilon_D$. We consequently repeat the Anderson-Morel calculation with a modified density of states, and show that in the

flat band limit we obtain a different result for the gap equation, and governed by a new energy scale.

5.1 Review of Anderson-Morel

In the Anderson-Morel model, the effect of two different interactions are looked at – an attractive phonon interaction λ and a repulsive Coloumb one μ. The latter acts over a much larger range of energies, while the first one acts over a small energy range ϵ_D near the Fermi surface. Hence the gap equation takes two different values, one within ϵ_D and the other between ϵ_D and the bandwidth W. Assuming a constant density of states N_0, this can be parametrized as

$$\begin{cases} N_0 V^e(\xi_k, \xi_{k'}) = \mu > 0 & \text{for} \quad |\xi_k|, |\xi_{k'}| \leq W \\ N_0 V^p(\xi_k, \xi_{k'}) = -\lambda < 0 & \text{for} \quad |\xi_k|, |\xi_{k'}| \leq \epsilon_D \end{cases}$$

where ξ_k is the electronic energy-dispersion relation.

Solving the self-consistent gap equation

$$\Delta(\xi_k) = -\int d\xi' N_0 V(\xi, \xi') \frac{\tanh(\beta\xi'/2)}{\xi'} \Delta(\xi') \tag{5.1}$$

then gives

$$\begin{pmatrix} \Delta_1 \\ \Delta_2 \end{pmatrix} = \begin{pmatrix} (\lambda - \mu)\ln(1.14\epsilon_D/k_BT) & -\mu\ln(W/\epsilon_D) \\ -\mu\ln(1.14\epsilon_D/k_BT) & -\mu\ln(W/\epsilon_D) \end{pmatrix} \begin{pmatrix} \Delta_1 \\ \Delta_2 \end{pmatrix}$$

Assuming non-zero values for the gap puts the following constraints on T_c

$$\begin{vmatrix} (\lambda - \mu)\ln(1.14\epsilon_D/k_BT) - 1 & -\mu\ln(W/\epsilon_D) \\ -\mu\ln(1.14\epsilon_D/k_BT) & -\mu\ln(W/\epsilon_D) - 1 \end{vmatrix} = 0$$

which gives

$$k_BT_c = 1.14\epsilon_D \exp\left(-\frac{1}{\lambda - \mu^*}\right) \quad \text{where} \quad \mu^* = \frac{\mu}{1 + \mu\ln(W/\epsilon_D)} \tag{5.2}$$

This is the result for a usual Fermi surface, where the Coloumb repulsion μ becomes dramatically renormalized to μ^*, by a factor that depends on the ratio of the bandwidth W to the Debye energy ϵ_D. As $W \gg \epsilon_D$ in this regime, the renormalized Coloumb repulsion becomes small such that the effective interaction is attractive – hence favoring superconductivity. In the following section, we consider what happens in the flat band limit when the flatband bandwidth $\Gamma_{FB} \ll \epsilon_D$.

5.2 In a partially flat band

We modify the density of states to reflect a flat band by including a large peak at the Fermi surface. Since the interaction is still only of two types (phonon and Coloumb), we still only have two values for the gap of Δ_1 and Δ_2. This is because the interaction is the only part of the sum in the gap equation Eq. 5.1 that depends on ξ (all other quantities depend on the internal index ξ').

Assuming that now we have a larger DOS αN_0 within a small energy window Γ_{FB}, where $\Gamma_{FB} \ll \epsilon_D$ and $\alpha > 1$, this gives us instead

$$\begin{vmatrix} (\lambda-\mu)\ln\left((1.14\Gamma_{FB}/k_BT)^{\alpha}\epsilon_D/\Gamma_{FB}\right)-1 & -\mu\ln(W/\epsilon_D) \\ -\mu\ln\left((1.14\Gamma_{FB}/k_BT)^{\alpha}\epsilon_D/\Gamma_{FB}\right) & -\mu\ln(W/\epsilon_D)-1 \end{vmatrix} = 0$$

which results in a modified gap equation

$$k_BT_c = 1.14\Gamma_{FB}\left(\frac{\epsilon_D}{\Gamma_{FB}}\right)^{\frac{1}{\alpha}} \exp\left(-\frac{1}{\alpha(\lambda-\mu^*)}\right) \tag{5.3}$$

where μ^* is defined in the same way as it was in the previous section.

We see that T_c is governed now by the energy scale of the flatband bandwidth Γ_{FB}, along with other pre-factors that modify the relation. It is intriguing whether this new relation can describe superconductivity in other materials which have partially flat bands, such as the heavy fermion materials.

Appendix A

Anyon superfluid properties

In this Appendix we consider the energy scales and additional technical details for the anyon superconductor proposal given in chapter three.

A.1 Estimation of anyon energy scales

The anyon interaction energy can estimated by the Coloumb repulsion between them, $\sim (e/3)^2/\epsilon l_a$. Their charge is $e/3$ and l_a is their interparticle spacing as determined by their density. ϵ gives the effective screening, e.g. is the dielectric constant of the underlying substrate.

As for the anyon hopping energy, we first look at Fig. A-1 for a reminder of key energy scales in this system: $\Delta \sim t$ for the typical electron hopping and W for the bandwidth of the flat band. As mentioned in the introduction, since an anyon has a magnetic length scale on the order of the lattice spacing here [1], it forms a strong local charge distortion (in contrast to anyons from a FQH state in semiconductor systems with much larger magnetic length scales hence only weakly distorting the wavefunction). In this case, since the anyon/electron interaction energy scale is similar to or larger than the bandgap Δ, the presence of an anyon can cause significant interband mixing. In this case, the anyon hopping will be determined by the typical electron hopping (also the scale of Δ), giving rise to an effective anyon mass from $t \sim \hbar^2/m_a a^2$; here a is the lattice spacing.

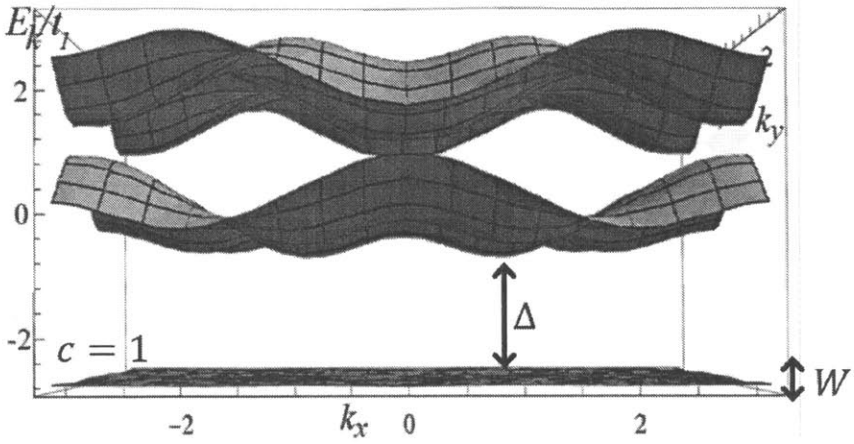

Figure A-1: Illustration of relevant energy scales in the flat band [1]: Δ is the bandgap and on the order of the typical electron hopping t, which we expect to govern the anyon hopping strength. This is distinct from the width of the flat band W — a finely tuned balance of several hopping and spin-orbit parameters.

Using this effective anyon mass m_a, we can now estimate the anyon kinetic energy, which is $\sim \hbar^2/m_a l_a^2$. This is an energy scale distinct from W, as the latter is a fine balance of different hopping parameters (e.g. the typical electron hopping and spin-orbit coupling) on a frustrated lattice, and anyons would reside on a separate unfrustrated lattice. The regime we are interested in is where the anyon kinetic energy dominates the anyon interaction energy.

A.2 Vortex quantization

Excitations of the zero mode can be described within our K-matrix theory as $\boldsymbol{l}$-vectors that overlap with the zero eigenvector in Eq. 3.9, for instance $\boldsymbol{l} = (1,0,0,0,0,0)^T$. As mentioned, this zero-mode is associated with a gapless Maxwell field a_μ as there is no Chern-Simons term. Here we examine its vortex quantization.

This excitation can be described with the following terms in the Lagrangian

$$\mathcal{L} = l_0 a_0 \delta(\mathbf{x}) + \frac{1}{2g}(E^2 - B^2)$$
$$+ e\mathbf{q}'\delta A_\mu \sum_i \frac{1}{2\pi}\partial_\nu a_{\lambda i}\epsilon^{\mu\nu\lambda} + ... \tag{A.1}$$

where $E_i = \partial_0 a_i - \partial_i a_0$ and $B_i = \partial_1 a_2 - \partial_2 a_1$. Here the charge vector $\mathbf{q} = \frac{1}{3}(1,1,1,1,1,1)$ couples the internal gauge-fields to the probe electromagnetic field, and $\mathbf{q}' = U^T\mathbf{q}$. We write l_0 as the first element in the vector $\boldsymbol{l}$ that couples to the a_0 component of the gauge-field. The first term in the expression above introduces an l_0 charge, the second is just the Maxwell term and the third couples the electromagnetic field to the internal gauge-fields (from Eq. 3.7).

Varying with respect to a_0, we obtain Gauss's Law:

$$\nabla \cdot \mathbf{E} = g l_0 \delta(\mathbf{x}) \tag{A.2}$$

This gives an electric field (see Fig. 3-2)

$$\mathbf{E} = \frac{g l_0}{2\pi}\frac{\mathbf{x}}{x^2} \tag{A.3}$$

that creates a density current since

$$J^\mu = \frac{1}{e}\frac{\partial \mathcal{L}}{\partial \delta A_\mu} = \frac{q_0'}{2\pi}\partial_\nu a_0 \epsilon^{\mu\nu 0}$$
$$= \frac{q_0'}{2\pi}E_\nu \epsilon^{\mu\nu 0} \tag{A.4}$$

where q_0' is the first element of the vector $\mathbf{q}'$ (as l_0 was defined previously). Combining this with the radially-directed electric field in Eq. A.3, we obtain

$$\mathbf{J} = \frac{q_0' g l_0}{(2\pi)^2}\frac{\hat{\theta}}{|\mathbf{x}|} \tag{A.5}$$

i.e. a circulating current around the charge couples to the probe field δA_μ (a vortex

as expected from the superfluid/$U(1)$ duality in 2+1 dimensions).

This vortex is quantized, as we can see by integrating the current around a loop

$$\begin{aligned} \oint d\mathbf{x} \cdot \mathbf{J} \frac{m}{\rho} &= \oint d\mathbf{x} \frac{l_0}{q_0'} \frac{\hat{\theta}}{|\mathbf{x}|} \\ &= 2\pi \frac{l_0}{q_0'} \end{aligned} \tag{A.6}$$

where m and ρ are the superfluid mass and density respectively. Their ratio can be converted to a quantity involving the gauge field couplings g and q_0' by comparing the dual terms in the action. The kinetic terms in the action for both the superfluid and $U(1)$ descriptions, $E^2/2g$ and $\frac{1}{2}mv^2\rho$ (v is the superfluid velocity), can be converted into each other using $j = v\rho$ and Eq. A.4. This gives $m/\rho = (2\pi q_0')^2/g$, which we use to obtain the result in Eq. A.6.

In all our examples, the flux quantization obtained is π/e, which corresponds to a superconducting vortex of $hc/2e$, similar to that in a BCS-type superconductor.

Appendix B

Symmetry analysis of Dirac point shifts in TCIs

Here we provide a derivation of the strain-induced gauge field (4.1), or equivalently Dirac point displacement on the (001) surface Brillouin zone of topological crystalline insulators. The derivation is based on symmetry analysis. A generic in-plane strain u_{ij} can be decomposed into three independent components: compression/dilation $u_{xx}+u_{yy}$, uniaxial stretch $u_{xx}-u_{yy}$, and shear $u_{xy}+u_{yx}$, which transform differently under crystal symmetries.

Compression/dilation preserves the full symmetry of the (001) surface. In particular, the presence of two mirror planes (110) and $(1\bar{1}0)$ guarantees the two pairs of Dirac points $\pm\mathbf{K}_1$ and $\pm\mathbf{K}_2$ lie along the mirror-invariant lines ΓX_1 and ΓX_2 respectively, in the surface Brillouin zone[26]. Importantly, the Dirac point positions on the ΓX lines are not constrained by symmetry[79]; they vary continuously under strain[115]. As shown in recent ab-initio calculations[92, 116], a compressive (tensile) strain moves $\pm\mathbf{K}_1$ and $\pm\mathbf{K}_2$ towards (away from) the Brillouin zone center Γ (see Fig.1b).

Uniaxial stretch in the $[1\bar{1}0]$ direction preserves both (110) and $(1\bar{1}0)$ mirror planes but breaks the four-fold symmetry: $u_{xx}-u_{yy}$ is odd under the $\pi/2$ rotation $x\to y$, $y\to -x$. As a consequence, the Dirac points $\pm\mathbf{K}_1$ and $\pm\mathbf{K}_2$ move along the ΓX lines by an equal distance but in opposite directions: $\pm\mathbf{K}_1$ move inward and $\pm\mathbf{K}_2$

move outward (see Fig.1c).

Shear strain breaks both (110) and $(1\bar{1}0)$ mirror symmetries, as well as the four-fold rotation symmetry. Therefore, Dirac points move perpendicular to the ΓX lines, and the displacement vector $\mathbf{K}_1' - \mathbf{K}_1$ is opposite to $\mathbf{K}_2' - \mathbf{K}_2$ after the $\pi/2$ rotation (see Fig.1d).

It follows from the above analysis that a generic strain-induced gauge field $\mathbf{A}_j$ acting on the Dirac fermion at valley $\mathbf{K}_j$ consists of contributions from compression/dilation, stretch and shear, which involve three independent coupling constants. Adding up the corresponding Dirac point displacements leads to the expression of $\mathbf{A}_j$ in (4.1). Note that the form of $\mathbf{A}_j$ in topologically crystalline insulators is different from its counter-part in graphene, which has been extensively studied in recent years[84, 85, 86, 83]. For example, unlike here, a dilation in graphene does not generate a gauge field due to the pinning of Dirac points at Brillouin zone corners. This difference arises from the important distinction in crystal symmetry and electronic topology.

Bibliography

[1] Evelyn Tang, Jia-Wei Mei, and Xiao-Gang Wen. High temperature fractional quantum hall states. *Phys. Rev. Lett.*, 106:236802, 2011.

[2] Evelyn Tang and Xiao-Gang Wen. Superconductivity with intrinsic topological order induced by pure coulomb interaction and time-reversal symmetry breaking. *Phys. Rev. B*, 88:195117, Nov 2013.

[3] Evelyn Tang and Liang Fu. Strain-induced partially flat band, helical snake states and interface superconductivity in topological crystalline insulators. *Nat Phys*, 10(12):964–969, 12 2014.

[4] N. Ya. Fogel, E. I. Buchstab, Yu. V. Bomze, O. I. Yuzephovich, A. Yu. Sipatov, E. A. Pashitskii, A. Danilov, V. Langer, R. I. Shekhter, and M. Jonson. Interfacial superconductivity in semiconducting monochalcogenide superlattices. *Phys. Rev. B*, 66:174513, Nov 2002.

[5] L. D. Landau. Theory of phase transformations i. *Phys. Z. Sowjetunion*, 11:26, 1937.

[6] L. D. Landau and E. M. Lifschitz. *Statistical Physics - Course of Theoretical Physics Vol 5.* Pergamon, London, 1958.

[7] D. C. Tsui, H. L. Stormer, and A. C. Gossard. Two-dimensional magnetotransport in the extreme quantum limit. *Phys. Rev. Lett.*, 48:1559–1562, 1982.

[8] R. B. Laughlin. Anomalous quantum hall effect: An incompressible quantum fluid with fractionally charged excitations. *Phys. Rev. Lett.*, 50:1395–1398, 1983.

[9] Xiao-Gang Wen. Vacuum degeneracy of chiral spin state in compactified spaces. *Phys. Rev. B*, 40:7387, 1989.

[10] Xiao-Gang Wen and Q. Niu. Ground state degeneracy of the FQH states in presence of random potentials and on high genus riemann surfaces. *Phys. Rev. B*, 41:9377, 1990.

[11] Frank Wilczek and A. Zee. Appearance of gauge structure in simple dynamical systems. *Phys. Rev. Lett.*, 52:2111, 1984.

[12] Xiao-Gang Wen. Topological orders in rigid states. *Int. J. Mod. Phys. B*, 4:239, 1990.

[13] Xiao-Gang Wen. Topological orders and edge excitations in FQH states. *Advances in Physics*, 44:405, 1995.

[14] Alexei Kitaev and John Preskill. Topological entanglement entropy. *Phys. Rev. Lett.*, 96:110404, 2006.

[15] Michael Levin and Xiao-Gang Wen. Detecting topological order in a ground state wave function. *Phys. Rev. Lett.*, 96:110405, 2006.

[16] Xie Chen, Zheng-Cheng Gu, and Xiao-Gang Wen. Local unitary transformation, long-range quantum entanglement, wave function renormalization, and topological order. *Phys. Rev. B*, 82:155138, Oct 2010.

[17] Eric Dennis, Alexei Kitaev, Andrew Landahl, and John Preskill. Topological quantum memory. *J. Math. Phys.*, 43:4452–4505, 2002.

[18] J. M. Leinaas and J. Myrheim. On the theory of identical particles. *Il Nuovo Cimento*, 37B:1, 1977.

[19] F. Wilczek. Quantum mechanics of fractional-spin particles. *Phys. Rev. Lett.*, 49:957, 1982.

[20] D. Arovas, J. R. Schrieffer, and F. Wilczek. Fractional statistics and the quantum hall effect. *Phys. Rev. Lett.*, 53:722–723, 1984.

[21] G. Moore and N. Read. *Nucl. Phys. B*, 360:362, 1991.

[22] Xiao-Gang Wen. Non-abelian statistics in the FQH states. *Phys. Rev. Lett.*, 66:802, 1991.

[23] A. Yu. Kitaev. Fault-tolerant quantum computation by anyons. *Ann. Phys. (N.Y.)*, 303:2–30, 2003.

[24] Chetan Nayak, Steven H. Simon, Ady Stern, Michael Freedman, and Sankar Das Sarma. Non-abelian anyons and topological quantum computation. *Rev. Mod. Phys.*, 80:1083, 2008.

[25] M. Z. Hasan and C. L. Kane. *Colloquium* : Topological insulators. *Rev. Mod. Phys.*, 82:3045–3067, Nov 2010.

[26] T. H. Hsieh, H. Lin, J. Liu, W. Duan, A. Bansil, and L. Fu. Topological crystalline insulators in the SnTe material class. *Nat. Commun.*, 3:982, 2012.

[27] Y. Tanaka, Zhi Ren, T. Sato, K. Nakayama, S. Souma, T. Takahashi, Kouji Segawa, and Yoichi Ando. Experimental realization of a topological crystalline insulator in snte. *Nat Phys*, 8(11):800–803, 11 2012.

[28] P. Dziawa, B. J. Kowalski, K. Dybko, R. Buczko, A. Szczerbakow, M. Szot, E. Łusakowska, T. Balasubramanian, B. M. Wojek, M. H. Berntsen, O. Tjernberg, and T. Story. Topological crystalline insulator states in pb1âĹŠxsnxse. *Nat Mater*, 11(12):1023–1027, 12 2012.

[29] Su-Yang Xu, Chang Liu, N. Alidoust, M. Neupane, D. Qian, I. Belopolski, J. D. Denlinger, Y. J. Wang, H. Lin, L. A. Wray, G. Landolt, B. Slomski, J. H. Dil, A. Marcinkova, E. Morosan, Q. Gibson, R. Sankar, F. C. Chou, R. J. Cava, A. Bansil, and M. Z. Hasan. Observation of a topological crystalline insulator phase and topological phase transition in pb1âĹŠxsnxte. *Nat Commun*, 3:1192, 11 2012.

[30] Yoshinori Okada, Maksym Serbyn, Hsin Lin, Daniel Walkup, Wenwen Zhou, Chetan Dhital, Madhab Neupane, Suyang Xu, Yung Jui Wang, R. Sankar, Fangcheng Chou, Arun Bansil, M. Zahid Hasan, Stephen D. Wilson, Liang Fu, and Vidya Madhavan. Observation of dirac node formation and mass acquisition in a topological crystalline insulator. *Science*, 341(6153):1496–1499, 2013.

[31] Junwei Liu, Timothy H. Hsieh, Peng Wei, Wenhui Duan, Jagadeesh Moodera, and Liang Fu. Spin-filtered edge states with an electrically tunable gap in a two-dimensional topological crystalline insulator. *Nat Mater*, 13(2):178–183, 02 2014.

[32] Chen Fang, Matthew J. Gilbert, and B Andrei Bernevig. Large-chern-number quantum anomalous hall effect in thin-film topological crystalline insulators. *Phys. Rev. Lett.*, 112:046801, Jan 2014.

[33] F. Zhang, X. Li, J. Feng, C. L. Kane, and E. J. Mele. Zeeman Field-Tuned Transitions for Surface Chern Insulators. *ArXiv e-prints*, September 2013.

[34] Hosho Katsura, Isao Maruyama, Akinori Tanaka, and Hal Tasaki. Ferromagnetism in the hubbard model with topological/non-topological flat bands. *EPL (Europhysics Letters)*, 91(5):57007, 2010.

[35] Dmitry Green, Luiz Santos, and Claudio Chamon. Isolated flat bands and spin-1 conical bands in two-dimensional lattices. *Phys. Rev. B*, 82:075104, Aug 2010.

[36] G. Liu, P. Zhang, Z. Wang, and S.-S. Li. Spin Hall effect on the kagome lattice with Rashba spin-orbit interaction. *Phys. Rev. B*, 79:035323, 2009.

[37] H.-M. Guo and M. Franz. Topological insulator on the kagome lattice. *Phys. Rev. B*, 80:113102, 2009.

[38] H.-M. Guo and M. Franz. Three-dimensional Topological Insulators on the Pyrochlore Lattice. *Phys. Rev. Lett.*, 103:206805, 2009.

[39] Z. Wang and P. Zhang. Quantum spin Hall effect and spin-charge separation in kagome lattice. 2009.

[40] K. Ohgushi, S. Murakami, and N. Nagaosa. Spin anisotropy and quantum hall effect in the kagome lattice - chiral spin state based on a ferromagnet. *Phys. Rev. B*, 62:6065, 2000.

[41] T. Kimura, H. Tamura, K. Shiraishi, and H. Takayanagi. Magnetic field effects on two-dimensional Kagome lattices. *Phys. Rev. B*, 65:081307, 2002.

[42] A. Tanaka and H. Ueda. Stability of Ferromagnetism in the Hubbard Model on the Kagome Lattice. *Phys. Rev. Lett.*, 90:067204, 2003.

[43] F. Pollmann, P. Fulde, and K. Shtengel. Kinetic ferromagnetism on a kagome lattice. *Phys. Rev. Lett.*, 100:136404, 2008.

[44] J. Wen, A. Rüegg, C.-C. J. Wang, and G. A. Fiete. Interaction-driven topological insulators on the kagome and the decorated honeycomb lattices. *Phys. Rev. B*, 82:075125, 2010.

[45] S. Rachel and K. Le Hur. Topological insulators and mott physics from the hubbard interaction. *Phys. Rev. B*, 82:075106, 2010.

[46] N. Hao, P. Zhang, and Y. Wang. Topological phases and fractional excitations of exciton condensate in electron-hole spintronic bilayer. 2010.

[47] Q. Liu, H. Yao, and T. Ma. Spontaneous symmetry breakings in two-dimensional kagome lattice. *Phys. Rev. B*, 82:045102, 2010.

[48] S. Nishimoto, M. Nakamura, A. O'Brien, and P. Fulde. Metal-insulator transition of the Kagome lattice fermions at 1/3 filling. 2010.

[49] Ivar Martin and C. D. Batista. Itinerant electron-driven chiral magnetic ordering and spontaneous quantum hall effect in triangular lattice models. *Phys. Rev. Lett.*, 101:156402, Oct 2008.

[50] D. J. Thouless, M. Kohmoto, M. P. Nightingale, and M. den Nijs. Quantized hall conductance in a two-dimensional periodic potential. *Phys. Rev. Lett.*, 49:405, 1982.

[51] Doron L. Bergman, Congjun Wu, and Leon Balents. Band touching from real-space topology in frustrated hopping models. *Phys. Rev. B*, 78:125104, Sep 2008.

[52] R. L. Willett, H. L. Stormer, D. C. Tsui, A. C. Gossard, and J. H. English. Uantitative experimental test for the theoretical gap energies in the fractional quantum Hall effect. *Phys. Rev. B*, 37:8476, 1988.

[53] A. Zorko, S. Nellutla, J. van Tol, L. C. Brunel, F. Bert, F. Duc, J. C. Trombe, M. A. de Vries, A. Harrison, and P. Mendels. Dzyaloshinsky-Moriya Anisotropy in the Spin-1/2 Kagomé Compound $ZnCu_3(OH)_6Cl_2$. *Phys. Rev. Lett.*, 101:026405, 2008.

[54] L. A. Fenner, A. A. Dee, and A. S. Wills. Non-collinearity and spin frustration in the itinerant kagome ferromagnet Fe3Sn2. *J. Phys.: Condens. Matter*, 21:452202, 2009.

[55] T. Kida, L. Fenner, A. S. Wills, I. Terasaki, and M. Hagiwara. Giant anomalous Hall resistivity of the room temperature ferromagnet Fe3Sn2 - a frustrated metal with the kagome-bilayer structure. 2009.

[56] Y.-J. Lin, R. L. Compton, K. J. Garcia, J. V. Porto, and I. B. Spielman. Synthetic magnetic fields for ultracold neutral atoms. *Nature*, 462:628, 2009.

[57] N. Goldman, I. Satija, P. Nikolic, A. Bermudez, M. A. Martin-Delgado, M. Lewenstein, and I. B. Spielman. Realistic Time-Reversal Invariant Topological Insulators With Neutral Atoms. 2010.

[58] Titus Neupert, Luiz Santos, Claudio Chamon, and Christopher Mudry. Fractional quantum hall states at zero magnetic field. *Phys. Rev. Lett.*, 106:236804, Jun 2011.

[59] Kai Sun, Zhengcheng Gu, Hosho Katsura, and S. Das Sarma. Nearly flatbands with nontrivial topology. *Phys. Rev. Lett.*, 106:236803, Jun 2011.

[60] D. N. Sheng, Z.-C. Gu, K. Sun, and L. Sheng. Fractional quantum Hall effect in the absence of Landau levels. *Nature*, 2:389, 2011.

[61] N. Regnault and B. Andrei Bernevig. Fractional chern insulator. *Phys. Rev. X*, 1:021014, Dec 2011.

[62] R. B. Laughlin. *Science*, 242:525, 1988.

[63] R. B. Laughlin. *Phys. Rev. Lett.*, 60:1057, 1988.

[64] A. Fetter, C. Hanna, and R. Laughlin. *Phys. Rev. B*, 39:9679, 1989.

[65] Yi-Hong Chen, Frank Wilczek, Edward Witten, and Bertrand I. Halperin. On anyon superconductivity. *Int. J. of Mod. Phys. B*, 03(07):1001–1067, 1989.

[66] S. M. Girvin and A. H. MacDonald. Off-diagonal long-range order, oblique confinement, and the fractional quantum hall effect. *Phys. Rev. Lett.*, 58:1252, 1987.

[67] S. C. Zhang, T. H. Hansson, and S. Kivelson. Effective-field-theory model for the fractional quantum hall effect. *Phys. Rev. Lett.*, 62:82, 1989.

[68] J. K. Jain. *Phys. Rev. Lett.*, 63:199, 1989.

[69] B. Blok and Xiao-Gang Wen. Effective theories of fractional quantum hall effect at generic filling fractions. *Phys. Rev. B*, 42:8133, 1990.

[70] B. Blok and Xiao-Gang Wen. Effective theories of fractional quantum hall effect: Hierarchical construction. *Phys. Rev. B*, 42:8145, 1990.

[71] Xiao-Gang Wen. *Quantum Field Theory of Many-Body Systems - From the Origin of Sound to an Origin of Light and Electrons.* Oxford Univ. Press, Oxford, 2004.

[72] B. I. Halperin. *Helv. Phys. Acta*, 56:75, 1983.

[73] Xiao-Gang Wen and A. Zee. Compressibility and superfluidity in the fractional-statistics liquid. *Phys. Rev. B*, 41:240, 1990.

[74] Xiao-Gang Wen and A. Zee. Neutral superfluid modes and "magnetic" monopoles in muti-layered FQH states. *Phys. Rev. Lett.*, 69:1811, 1992.

[75] Zhenghan Wang. *Topological Quantum Computation.* CBMS Regional Conference Series in Mathematics, 2010.

[76] Xiao-Liang Qi. Generic wave-function description of fractional quantum anomalous hall states and fractional topological insulators. *Phys. Rev. Lett.*, 107:126803, Sep 2011.

[77] Xiao-Liang Qi and Shou-Cheng Zhang. Topological insulators and superconductors. *Rev. Mod. Phys.*, 83:1057–1110, Oct 2011.

[78] Joel E. Moore. The birth of topological insulators. *Nature*, 464(7286):194–198, 03 2010.

[79] Junwei Liu, Wenhui Duan, and Liang Fu. Two types of surface states in topological crystalline insulators. *Phys. Rev. B*, 88:241303, Dec 2013.

[80] Liang Fu. Topological crystalline insulators. *Phys. Rev. Lett.*, 106:106802, Mar 2011.

[81] Roger S. K. Mong, Andrew M. Essin, and Joel E. Moore. Antiferromagnetic topological insulators. *Phys. Rev. B*, 81:245209, Jun 2010.

[82] Y. Tanaka, T. Sato, K. Nakayama, S. Souma, T. Takahashi, Zhi Ren, M. Novak, Kouji Segawa, and Yoichi Ando. Tunability of the k-space location of the dirac cones in the topological crystalline insulator $pb_{1-x}sn_xte$. *Phys. Rev. B*, 87:155105, Apr 2013.

[83] N. Levy, S. A. Burke, K. L. Meaker, M. Panlasigui, A. Zettl, F. Guinea, A. H. Castro Neto, and M. F. Crommie. Strain-induced pseudo?magnetic fields greater than 300 tesla in graphene nanobubbles. *Science*, 329(5991):544–547, 2010.

[84] J. L. Mañes. Symmetry-based approach to electron-phonon interactions in graphene. *Phys. Rev. B*, 76:045430, Jul 2007.

[85] F. Guinea, M. I. Katsnelson, and A. K. Geim. Energy gaps and a zero-field quantum hall effect in graphene by strain engineering. *Nat Phys*, 6(1):30–33, 01 2010.

[86] Vitor M. Pereira and A. H. Castro Neto. Strain engineering of graphene's electronic structure. *Phys. Rev. Lett.*, 103:046801, Jul 2009.

[87] A. Yu. Sipatov. *Functional Materials.*

[88] L. S. Palatnik and A. I. Fedorenko. *J. Cryst. Growth.*

[89] G. Springholz and K. Wiesauer. Nanoscale dislocation patterning in PbTe/PbSe(001) lattice-mismatched heteroepitaxy. *Phys. Rev. Lett.*, 88:015507, Dec 2001.

[90] P. Chaikin and C. L. Lubensky. *Principles of Condensed Matter Physics.* Cambridge University Press, Cambridge, 2000.

[91] M. J. Weber. *Handbook of Optical Materials.* CRC Press, 2002.

[92] Paolo Barone, Domenico Di Sante, and Silvia Picozzi. Strain engineering of topological properties in lead-salt semiconductors. *physica status solidi (RRL) âĂŞ Rapid Research Letters*, 7(12):1102–1106, 2013.

[93] Dmitri B. Chklovskii and Patrick A. Lee. Transport properties between quantum hall plateaus. *Phys. Rev. B*, 48:18060–18078, Dec 1993.

[94] Liang Fu and C. L. Kane. Topology, delocalization via average symmetry and the symplectic anderson transition. *Phys. Rev. Lett.*, 109:246605, Dec 2012.

[95] K. Murase, S. Ishida, S. Takaoka, T. Okumura, H. Fujiyasu, A. Ishida, and M. Aoki. Superconducting behavior in pbteîŮÿsnte superlattices. *Surface Science*, 170(1âĂŞ2):486 – 490, 1986.

[96] A. Yu. Sipatov A. I. Fedorenko A. N. Chirkin S. V. Chistyakov O. A. Mironov, A. B. Savitskii and L. P. Shpakovskaya. *JETP Lett.*

[97] D. Agassi and T. K. Chu. Strain-induced superconductivity in lead salt superlattices. *physica status solidi (b)*, 160(2):601–611, 1990.

[98] N. Ya. Fogel, E. I. Buchstab, Yu. V. Bomze, O. I. Yuzephovich, M. Yu. Mikhailov, A. Yu. Sipatov, E. A. Pashitskii, R. I. Shekhter, and M. Jonson. Direct evidence for interfacial superconductivity in two-layer semiconducting heterostructures. *Phys. Rev. B*, 73:161306, Apr 2006.

[99] O. I. Yuzephovich, M. Yu. Mikhailov, S. V. Bengus, A. Yu. Aladyshkin, E. E. Pestov, Yu. N. Nozdrin, A. Yu. Sipatov, E. I. Buchstab, and N. Ya. Fogel. Interfacial superconductivity in bilayer and multilayer ivâĂŞvi semiconductor heterostructures. *Low Temperature Physics*, 34(12), 2008.

[100] N. Ya. Fogel, A. S. Pokhila, Yu. V. Bomze, A. Yu. Sipatov, A. I. Fedorenko, and R. I. Shekhter. Novel superconducting semiconducting superlattices: Dislocation-induced superconductivity? *Phys. Rev. Lett.*, 86:512–515, Jan 2001.

[101] N. B. Kopnin, T. T. Heikkilä, and G. E. Volovik. High-temperature surface superconductivity in topological flat-band systems. *Phys. Rev. B*, 83:220503, Jun 2011.

[102] V. Khodel and V. Shaginyan. *JETP Lett.*

[103] R. Yoshimi, A. Tsukazaki, K. Kikutake, J. G. Checkelsky, K. S. Takahashi, M. Kawasaki, and Y. Tokura. Dirac electron states formed at the heterointerface between a topological insulator and a conventional semiconductor. *Nat Mater*, 13(3):253–257, 03 2014.

[104] C. Panagopoulos J. Pereiro, A. Petrovic and I. Bozovic. *Physics Express.*

[105] Zhang Wen-Hao, Sun Yi, Zhang Jin-Song, Li Fang-Sen, Guo Ming-Hua, Zhao Yan-Fei, Zhang Hui-Min, Peng Jun-Ping, Xing Ying, Wang Hui-Chao, Fujita Takeshi, Hirata Akihiko, Li Zhi, Ding Hao, Tang Chen-Jia, Wang Meng, Wang Qing-Yan, He Ke, Ji Shuai-Hua, Chen Xi, Wang Jun-Feng, Xia Zheng-Cai, Li Liang, Wang Ya-Yu, Wang Jian, Wang Li-Li, Chen Ming-Wei, Xue Qi-Kun, and Ma Xu-Cun. Direct observation of high-temperature superconductivity in one-unit-cell fese films. *Chinese Physics Letters*, 31(1):017401, 2014.

[106] Pouyan Ghaemi, Jérôme Cayssol, D. N. Sheng, and Ashvin Vishwanath. Fractional topological phases and broken time-reversal symmetry in strained graphene. *Phys. Rev. Lett.*, 108:266801, Jun 2012.

[107] Michael Levin and Ady Stern. Fractional topological insulators. *Phys. Rev. Lett.*, 103:196803, Nov 2009.

[108] Bitan Roy, Fakher F. Assaad, and Igor F. Herbut. Zero modes and global antiferromagnetism in strained graphene. *Phys. Rev. X*, 4:021042, May 2014.

[109] Hongming Weng, Jianzhou Zhao, Zhijun Wang, Zhong Fang, and Xi Dai. Topological crystalline kondo insulator in mixed valence ytterbium borides. *Phys. Rev. Lett.*, 112:016403, Jan 2014.

[110] M. Ye, J. W. Allen, and K. Sun. Topological crystalline Kondo insulators and universal topological surface states of SmB$_6$. *ArXiv e-prints*, July 2013.

[111] Mehdi Kargarian and Gregory A. Fiete. Topological crystalline insulators in transition metal oxides. *Phys. Rev. Lett.*, 110:156403, Apr 2013.

[112] M. Kindermann. Topological crystalline insulator phase in graphene multilayers. *Phys. Rev. Lett.*, 114:226802, Jun 2015.

[113] Timothy H. Hsieh, Junwei Liu, and Liang Fu. Topological crystalline insulators and dirac octets in antiperovskites. *Phys. Rev. B*, 90:081112, Aug 2014.

[114] P. Morel and P. W. Anderson. Calculation of the superconducting state parameters with retarded electron-phonon interaction. *Phys. Rev.*, 125:1263–1271, Feb 1962.

[115] Maksym Serbyn and Liang Fu. Symmetry breaking and landau quantization in topological crystalline insulators. *Phys. Rev. B*, 90:035402, Jul 2014.

[116] Xiaofeng Qian, Liang Fu, and Ju Li. Topological crystalline insulator nanomembrane with strain-tunable band gap. *Nano Research*, 8(3):967–979, 2015.